CHAPTER 2

MATHEMATICAL MODELS FOR IN-LINE HOLOGRAPHY: CONTINUOUS AND DISCRETE CASES

2.1. Introduction

Mathematical models for continous in-line holography can be found in the literature [1,32]. The systems approach, which models the physical phenomena using filters and other elements which have an input-output description, is emphasized in this dissertation. It is very useful to model holography as a system whose elements are well known, such as filters, Fourier transformers, vector multipliers, etc. This approach gives a better presentation and makes it easier to apply the results of the many fields in the broad area of system science to holography. Furthermore, this approach simplifies the transition to discrete case and gives hints about efficient computational implementations. Such a model is presented in this chapter for Fresnel in-line holography.

Although not used later in this dissertation, the simplification of the model for the far-field (Fraunhofer) case is also presented.

Digital processing of holograms and digital simulation of holography require discrete models. In this chapter, two complete and working discrete models for Fresnel in-line holography are presented which utilize the systems approach. In order to give complete interpretatations of the discrete models, and to show their relationship to the continuous case, a detailed analysis of sampling rate effects is also included. The implementations of the models are given together with sample results. The discrete models presented in this chapter are the basis for the overall work in this dissertation.

Finally, an extension is made to multiple exposure holography, and simulation results are shown.

2.2. Continuous Domain Modelling

2.2.1. Recording

The mathematical model given in this section is based on the simplified diagram of Fig.3. The object distribution in the plane located at the origin (object plane) is represented by the object function $a(x,y)$. The object plane is illuminated by a plane wave. Therefore, the field just after the object plane is given by $1-a(x,y)$. Using Huygens-Fresnel approximation, the field distribution at a distance z from the object plane can be found as,

$$\psi_z(x,y) = B\int_{-\infty}^{\infty}\int_{-\infty}^{\infty}\left[1-a(\xi,\eta)\right]\left\{\frac{1}{j\lambda z}\exp\left[j\frac{\pi}{\lambda z}[(x-\xi)^2+(y-\eta)^2]\right]\right\} d\xi\, d\eta, \qquad (2.1)$$

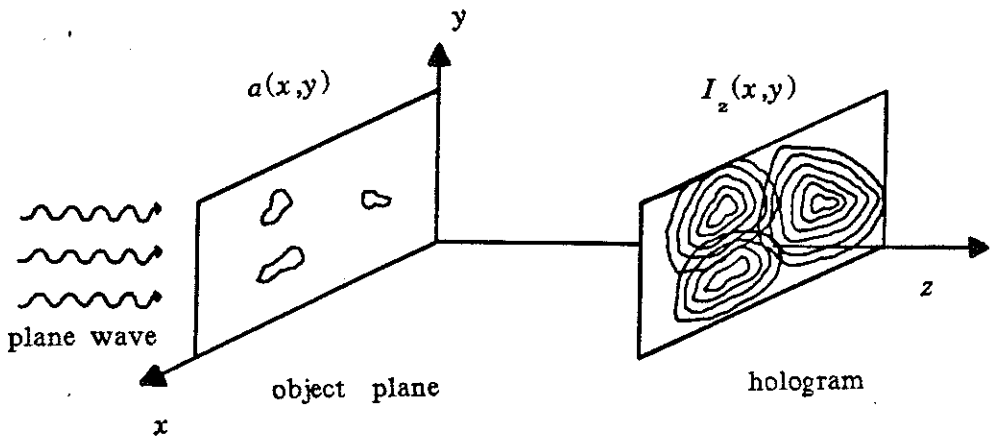

Figure 3. Hologram formation.

where, B is the amplitude of the illumination (assumed to be 1 from now on), and λ is the wavelength. The intensity of $\psi_z(x,y)$ is recorded as the hologram (in-line Fresnel hologram) $I_z(x,y)$, i.e.,

$$I_z(x,y) = \psi_z(x,y)\psi_z^*(x,y) = \left|\psi_z(x,y)\right|^2. \tag{2.2}$$

Defining

$$h_z(x,y) = \frac{1}{j\lambda z} \exp\left[j\frac{\pi}{\lambda z}(x^2+y^2)\right], \tag{2.3}$$

equation (2.1) can be written as:

$$\psi_z(x,y) = \left[1 - a(x,y)\right] ** h_z(x,y), \tag{2.4}$$

where, ** denotes two-dimensional convolution. Since the field is represented as a two-dimensional convolution, it can be modelled as the output of a two-dimensional linear system, where the system impulse function is $h_z(x,y)$. The block diagram of the system corresponding to hologram recording is shown in Fig.4. Note that $1 ** h_z(x,y) = 1$. Therefore,

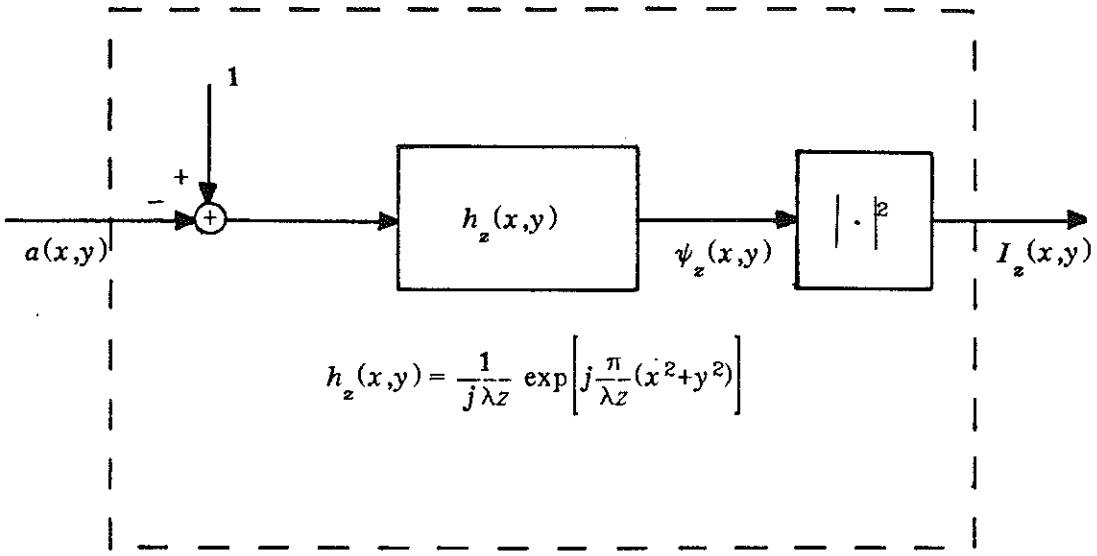

Figure 4. two-dimensional system model for hologram recording.

$$\begin{aligned} \psi_z(x,y) &= \left[1 - a(x,y)\right] ** h_z(x,y), \\ &= 1 ** h_z(x,y) - a(x,y) ** h_z(x,y), \\ &= 1 - a(x,y) ** h_z(x,y). \end{aligned} \tag{2.5}$$

The hologram $I_z(x,y)$, can then be written as:

$$I_z(x,y) = \left|1 - a(x,y) ** h_z(x,y)\right|^2. \tag{2.6}$$

Expanding the magnitude square operation, we get,

$$I_z(x,y) = 1 - a^*(x,y) ** h_z^*(x,y) - a(x,y) ** h_z(x,y) + \left|a(x,y) ** h_z(x,y)\right|^2. \tag{2.7}$$

Although it will be more clear after the section covering the reconstruction, it is worth noting here that the second and third terms (linear terms) are of extreme importance, since those are the ones which make it possible to reconstruct the hologram and generate the twin-image. The fourth term is called the cross-term, which is not desirable. The convolution with the kernel $h_z(x,y)$ is an operation which disperses the energy of a space limited smooth object $a(x,y)$ to a wider region in the x,y plane (wider as z becomes larger). If the energy of $a(x,y)$ is limited, then the energy of the linear terms of eq.(2.7) drops much below 1, everywhere, if z is sufficiently large. Therefore, the squares of these small values (the cross-term) are negligible. For passive objects (i.e. if the object does not amplify the incoming illumination and if it is not a source of illumination itself), which block only a small portion of the incoming illumination, the argument is correct even for moderate values of z which are not large enough to satisfy the far-field condition. Therefore, the cross-term is negligible for most practical cases, both for far-field and Fresnel holograms.

Another interpretation and a corresponding system model for in-line holography is possible because of the specific properties of the convolution kernel $h_z(x,y)$. The convolution given in eq.(2.5) can be rewritten by expanding the quadratic phase of $h_z(x,y)$ as follows:

$$\psi_z(x,y) = \frac{1}{j\lambda z}\int_{-\infty}^{\infty}\int_{-\infty}^{\infty}\left[1-a(\xi,\eta)\right]\exp\left[j\frac{\pi}{\lambda z}[x^2+y^2+\xi^2+\eta^2-2\xi x-2\eta y]\right],$$

$$= \frac{1}{j\lambda z}\exp\left[j\frac{\pi}{\lambda z}(x^2+y^2)\right]$$

$$\int_{-\infty}^{\infty}\int_{-\infty}^{\infty}\left[1-a(\xi,\eta)\right]\exp\left[j\frac{\pi}{\lambda z}(\xi^2+\eta^2)\right]\exp\left[-j\frac{2\pi}{\lambda z}(\xi x+\eta y)\right]\,d\xi d\eta\,, \tag{2.8}$$

$$= j\lambda z\; h_z(x,y)\;\mathcal{F}\left\{\left[1-a(\xi,\eta)\right]h_z(\xi,\eta)\right\},$$

where, $\mathcal{F}$ denotes two-dimensional continuous Fourier transform with the transform domain variables $\frac{2\pi}{\lambda z}x$ and $\frac{2\pi}{\lambda z}y$, throughout section 2. Thus, the hologram, $I_z(x,y)$, is,

$$I_z(x,y) = \left|\psi_z(x,y)\right|^2 = \left|j\lambda z h_z(x,y)\,\mathcal{F}\left\{\left[1-a(\xi,\eta)\right]h_z(\xi,\eta)\right\}\right|^2 = \left|\mathcal{F}\left\{\left[1-a(\xi,\eta)\right]h_z(\xi,\eta)\right\}\right|^2, \tag{2.9}$$

which is obtained by using $|h_z(x,y)| = \frac{1}{\lambda z}$. The system block diagram for this interpretation is given in Fig.5.

2.2.2. Reconstruction

Conventionally, the reconstruction is performed by reilluminating the developed hologram plate with the same coherent illumination, and imaging in the same plane as the hologram was originally recorded. Thus, this procedure is equivalent to replacing $a(x,y)$ (or $1-a(x,y)$ depending on negative or positive plate used) of eq.(2.1) by its hologram $I(x,y)$ multiplied by –1. The reconstruction can be easily demonstrated by noting the two

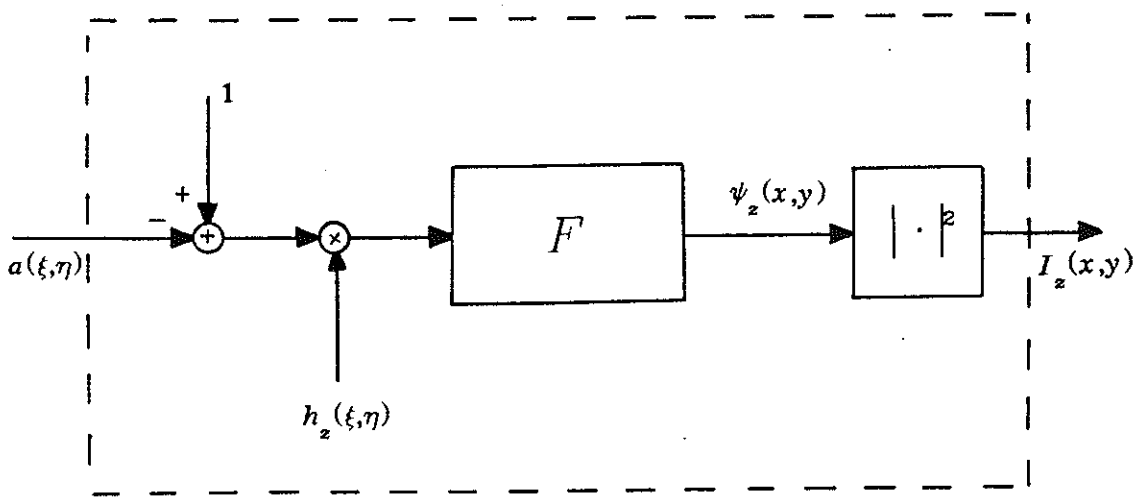

Figure 5. Another system model for in-line holography.

properties of the convolution kernel $h_z(x,y)$:

$$h_z(x,y) \;**\; h_z^*(x,y) = \delta(x,y), \tag{2.10.a}$$

$$h_z(x,y) \;**\; h_z(x,y) = h_{2z}(x,y). \tag{2.10.b}$$

Therefore, the field after the reconstruction, $\varphi_z(x,y)$, is:

$$\varphi_z(x,y) = 1 + I_z(x,y) \;**\; h_z(x,y). \tag{2.11}$$

Substituting eq.(2.7) into equation above, and again using $1 ** h_z(x,y) = 1$, yields,

$$\varphi_z(x,y) = 2 - a^*(x,y) ** h_z^*(x,y) ** h_z(x,y) - a(x,y) ** h_z(x,y) ** h_z(x,y)$$

$$(cross-term) ** h_z(x,y) ,$$

$$= 2 - a^*(x,y) ** \delta(x,y) - a(x,y) ** h_{2z}(x,y) + non-linear\ terms, \quad (2.12)$$

$$= 1 - a^*(x,y) + \left[1 - a(x,y) ** h_{2z}(x,y)\right] + non-linear\ terms,$$

$$= 1 - a^*(x,y) + \psi_{2z}(x,y) + non-linear\ terms.$$

Note that the second term (sometimes together with the preceding DC) is the desired reconstruction. The third term is the field of the hologram of the object distribution $a(x,y)$ at a distance $2z$. (Twice the distance of the original recording.) This term is called the twin-image effect. As indicated before, the non-linear terms are negligible for most of the cases. It is possible to use the conjugate kernel to get $a(x,y)$ instead of $a^*(x,y)$. In optical reconstructions only the intensity can be recorded. Therefore, a magnitude square operation is necessary to complete the analysis which will generate new undesired cross terms. In some non-optical reconstructions (such as digital) it may be possible to record the field.

It must be noted that in the case of intensity recording, the DC level of the hologram $I_z(x,y)$ (or equivalently the DC level of the reconstructed field) can be intentionally altered to get some specific results. One of the two extremes is adding a large DC so that the non-linear terms generated by the "magnitude square" operation are supressed and linear terms becomes dominant, i.e. if,

$$\varphi_z(x,y) = DC - a^*(x,y) + \psi_{2z}(x,y) + other\ terms, \quad (2.13)$$

then the intensity of the reconstruction, $R_z(x,y)$ is:

$$\begin{aligned} R_z(x,y) &= \varphi_z(x,y)\varphi_z^*(x,y) \ , \\ &= DC^2 - 2\mathrm{Re}\{ DC\ a(x,y) \} - 2\mathrm{Re}\{ DC\ \psi_{2z}(x,y) \} \\ &\quad + \left| a(x,y) \right|^2 + \left| \psi_{2z}(x,y) \right|^2 + \textit{other terms.} \end{aligned} \tag{2.14}$$

If DC is large, then non-linear terms including the intensity of the desired reconstruction are negligible. The dominant terms are the real part of the desired reconstructed object field and the real part of the twin-image field. On the other hand, one may completely eliminate the DC term (by setting $DC = 0$). In this case the intensity of the original object is reconstructed, together with the intensity of the contaminating twin-image and other non-linear terms. Either of the two extreme cases, as well as any other choice of DC may be desirable for some specific application. High DC level may create a problem of visibility in optical holography: the DC^2 term in the reconstruction (see eq.(2.14)) may get too high and consequently the visibility may get very poor. However, this is not a problem in digital reconstructions since the DC level can be very easily modified at any time.

2.2.3. Simplification of the model for far-field (Fraunhofer) case

Using the property,

$$\mathcal{F}\left\{ h_z(\xi,\eta) \right\} = -j\lambda z h_z^*(x,y) \ , \tag{2.15}$$

eq (2.8) can be written as,

$$\psi_z(x,y) = j\lambda z\, h_z(x,y)\left[\mathcal{F}\left\{h_z(\xi,\eta)\right\} - \mathcal{F}\left\{a(\xi,\eta)h_z(\xi,\eta)\right\}\right]$$

$$= -(j\lambda z)^2 h_z(x,y)h_z^*(x,y) - j\lambda z h_z(x,y)\mathcal{F}\left\{a(\xi,\eta)h_z(\xi,\eta)\right\}, \qquad (2.16)$$

$$= 1 - j\lambda z h_z(x,y)\mathcal{F}\left\{a(\xi,\eta)h_z(\xi,\eta)\right\} .$$

An observation based on eq.(2.16) is that the field, $\psi_z(x,y)$, is a kind of two-dimensional amplitude modulation (DC shifted), where the modulated signal (carrier) is the quadratic phase function, $j\lambda z h_z(x,y) = \exp\left[\frac{\pi}{\lambda z}(x^2+y^2)\right]$, and the modulating signal is the Fourier transform given in eq.(2.16). Note that both the carrier and the modulating signal are complex. If $a(\xi,\eta)$ is spatially limited in a small region such that $h_z(\xi,\eta)$ is almost constant ($h_z(\xi,\eta) \approx \frac{1}{j\lambda z}$) within the extent of $a(\xi,\eta)$ (far-field assumption), then eq.(2.16) can be simplified to yield,

$$\psi_z(x,y) = 1 - h_z(x,y)\mathcal{F}\left\{a(\xi,\eta)\right\} ,$$

$$= 1 - h_z(x,y)A\left(\frac{2\pi}{\lambda z}x, \frac{2\pi}{\lambda z}y\right) , \qquad (2.17)$$

where A is the two-dimensional Fourier transform of $a(\xi,\eta)$. The intensity of the field gives the far-field in-line hologram as,

$$I_z(x,y) = \psi_z(x,y)\psi_z^*(x,y) ,$$

$$= 1 - 2Re\left\{h_z(x,y)A\left(\frac{2\pi}{\lambda z}x,\frac{2\pi}{\lambda z}y\right)\right\} + \left|h_z(x,y)A\left(\frac{2\pi}{\lambda z}x,\frac{2\pi}{\lambda z}y\right)\right|^2 . \quad (2.18)$$

The far-field (Fraunhofer) approximation is not considered throughout this dissertation. Later, it will be shown that the Fresnel approximation is already simple enough for efficient computational simulations, In fact, the additional computational effort is minimal, and the benefits in turn are significant, since Fresnel holograms are frequently encountered; also the Fresnel formulation already embraces the far-field case.

2.2.4. Extension to three-dimensional case

Modelling and analysis throughout this dissertation are carried out for two-dimensional object distributions. However, it is pointed out in Chapter 1 that the main use of holography is to analyze object distributions in three-dimensional space. The extension of the modelling and analysis given above to the three-dimensional object distribution case is based on the assumption that the objects floating in a large volume of space are small in dimension such that multiple diffractions are negligible. In other words, illumination falling upon any object is a plane wave (the previously diffracted wave illuminating another object is negligible compared to plane wave illumination) no matter where the object is located. In this case, the three-dimensional volume can be thought to consist of two-dimensional slices; each slice generates its corresponding field at the recording (hologram) plane, and because of the assumption above, the field corresponding to each slice can be found using the model given in section 2.1. Since each slice is located at a different distance z from the recording plane, the corresponding convolution kernels, $h_z(x,y)$, have a different distance parameter z. The intensity of the combined field has the same linear terms for each slice as given for only one two-dimensional object distribution in section

2.1. Therefore, the reconstruction explained in section 2.2 is still valid, but a specific slice is imaged at a time, corresponding to the parameter z of the kernel used for reconstruction. However, reconstruction[1] of a specific plane also includes "out of focus" reconstruction of the other slices, which may become disturbing. The full three-dimensional distribution can be reconstructed repeating the reconstruction process for each slice (focusing).

2.3. Discrete Domain Modelling

2.3.1. Sampling rate requirement for in-line holograms

The main purpose of this work is to extract the object distribution $a(x,y)$ from their holograms digitally. In order to accomplish this task, first the holograms must be digitized, so that they can be transferred to a computer. Sampling rate (rectangular sampling is assumed) must be chosen such that most (ideally all) of the information related to the object distribution is preserved. Naturally, the frequency band of the hologram must be known in order to determine the sampling rate. Since the field $\psi_z(x,y)$ is the output of a linear system, its frequency band is the intersection of the band of system impulse function $h_z(x,y)$, and that of the input, $1 - a(x,y)$, i.e.,

$$band\ of\ \psi_z(x,y) = band\ of\ h_z(x,y) \cap band\ of\ \left[1 - a(x,y)\right] . \qquad (2.19)$$

The system impulse function $h_z(x,y)$ is not band limited. Therefore, the frequency band of $\psi_z(x,y)$ is exactly equal to the frequency band of $1 - a(x,y)$. The immediate result of this observation is that if the input object distribution is bandlimited, then $\psi_z(x,y)$ can be

---

[1] The term "reconstruction" as used in this paragraph is not a good usage for optical reconstruction process, since what is reconstructed is only the wave front. The reconstructed wave front is then "imaged" at different distances. However, the digital case is conceptually different since there is no significance of a wave front. Instead, depending on the convolution kernel used, the images of individual planes are obtained directly from the hologram. Thus each of them can be considered as a seperate "reconstruction" at a certain distance. The term "reconstruction" is used in this second sense throughout this dissertation.

sampled without losing any information, at a rate higher than the Nyquist rate of $a(x,y)$. Since $I_z(x,y) = \psi_z(x,y)\psi_z^*(x,y)$, its Fourier transform, $I(u,v)$ (transform domain variables are u and v) is given by,

$$I(u,v) = \Psi_z(u,v) ** \Psi_z^*(-u,-v) , \tag{2.20}$$

where $\Psi_z(u,v)$ is the Fourier transform of $\psi_z(x,y)$. Therefore, $I_z(x,y)$ is band limited, but its upper frequency limits are twice that of $\psi_z(x,y)$, and that of $a(x,y)$. The frequency bands occupied by individual terms of $I_z(x,y)$ (see eq.(2.7)), can be easily seen from Fig.6. The linear important terms of $I_z(x,y)$ occupy the same band as $a(x,y)$. Since the cross-term is negligible most of the time and since it is an undesirable term anyway, there is no need to determine the sampling rate according to its bandwidth. Therefore, the sampling rate requirement for in-line holograms is the **same** as that of the input $a(x,y)$, in order not to lose any information related to input object, due to sampling. The sampling rate requirement of $a(x,y)$ (equivalently the frequency band of it) can be determined from either physical considerations or the desired resolution. In applications where it is desirable to keep the cross-term, the sampling rate requirement is twice of that of $a(x,y)$. Undersampling results in aliasing as usual.

2.3.2. Digital simulation of in-line holography (Type I)

The digital simulation of in-line holography (recording and/or reconstruction) requires the digital implementation of either one of the continuous systems shown in Figs.4 and 5. The one which implements the system of Fig.4 is denoted as Type I in this dissertation, whereas the other one is called Type II.

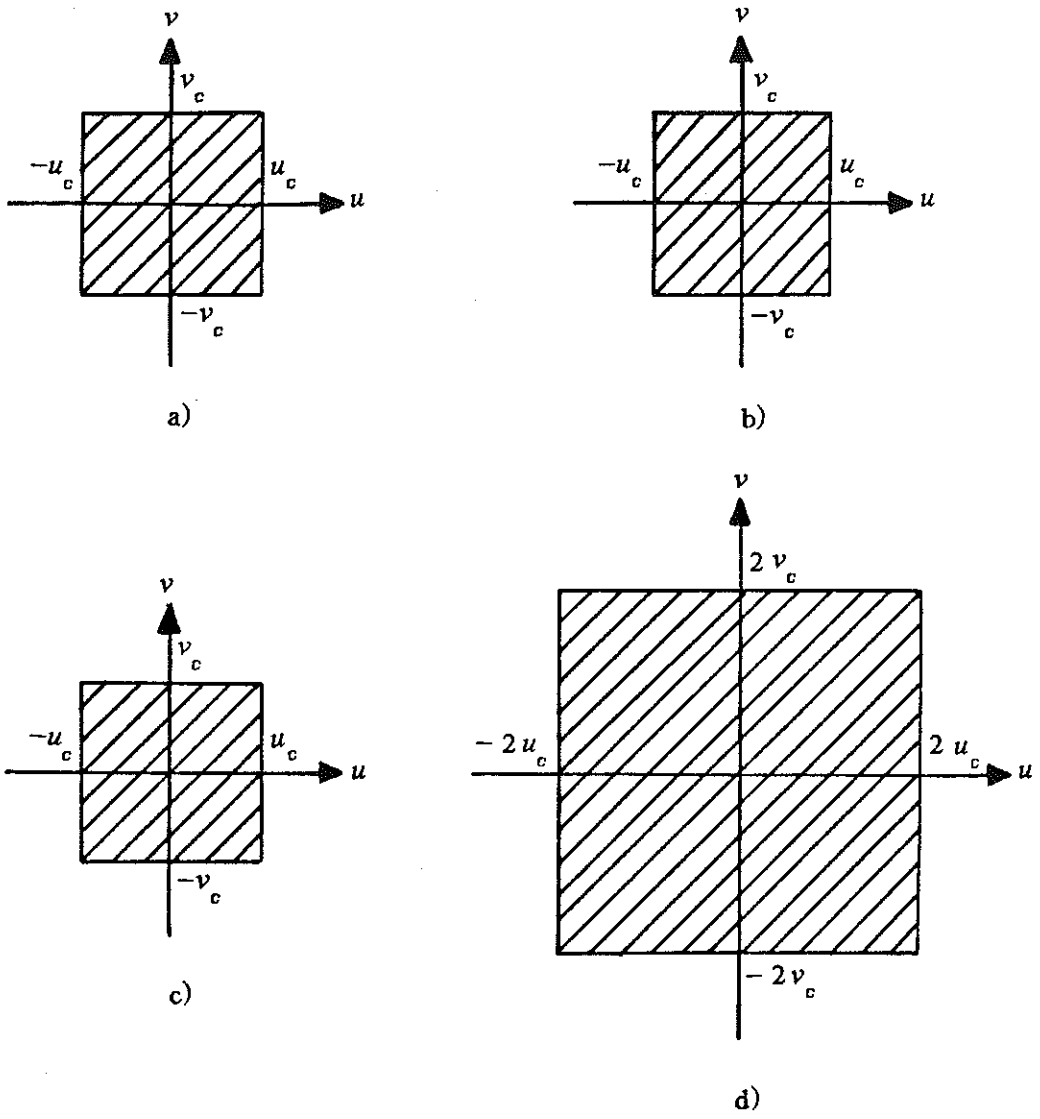

Figure 6. Frequency bands occupied by different components of hologram, a) Assumed band of the input object distribution $a(x,y)$, b) Band of $a^*(x,y)$ ** $h_z^*(x,y)$, given a, c) Band of $a(x,y)$ ** $h_z(x,y)$, given a, d) Band of $|a(x,y)$ ** $h_z(x,y)|^2$, given a.

Lets consider the system given in Fig.4. A discrete system impulse function $h_{zD}(n,m)$ must be determined corresponding to the continuous impulse function $h_z(x,y)$.

As already mentioned, the system impulse function $h_z(x,y)$ is neither band-limited nor space-limited. Lets define that the function $a_{LP}(x,y)$ is obtained from the original

input function $a(x,y)$, by passing it through an ideal low-pass filter with cut-off frequencies u_c and v_c, i.e.,

$$a_{LP}(x,y) = a(x,y) ** g_{LP}(x,y) \ . \tag{2.21}$$

Let us suppose that this band-limited function, $a_{LP}(x,y)$, is the input to the recording system. Then the field, $\psi_z(x,y)$, is,

$$\begin{aligned} \psi_z(x,y) &= \left[1 - a_{LP}(x,y)\right] ** h_z(x,y) \ , \\ &= \left[1 - a(x,y)\right] ** g_{LP}(x,y) ** h_z(x,y) \ , \end{aligned} \tag{2.22}$$

Now, define

$$h_{zLP}(x,y) = g_{LP}(x,y) ** h_z(x,y) \ . \tag{2.23}$$

Thus,

$$\psi_z(x,y) = \left[1 - a(x,y)\right] ** h_{zLP}(x,y) \ . \tag{2.24}$$

What is shown above is, in fact, the direct consequence of linearity: the assumption that the input is band-limited is equivalent to the assumption that the system is band-limited. Therefore, the discrete system impulse function can be obtained from the continuous system impulse function by sampling it at a rate determined as discussed in section 2.3.1.

Another observation is based on the fact that the band-limited system function $h_{zLP}(x,y)$, drops quickly to zero beyond some spatial limit x_c and y_c. In other words, it is *almost* space-limited. This can be shown from the linear instantenous frequency, i.e.,

$$\begin{aligned} h_z(x,y) &= c\ \exp\{j\,\phi(x,y)\} \\ u_i &\equiv \frac{d\,\phi}{dx} = \frac{\pi}{\lambda z}2x \\ v_i &\equiv \frac{d\,\phi}{dy} = \frac{\pi}{\lambda z}2y. \end{aligned} \tag{2.25}$$

So, the approximate cut-off points in space are,

$$\begin{aligned} x_c &= \pm\frac{\lambda z}{2\pi}u_c, \\ y_c &= \pm\frac{\lambda z}{2\pi}v_c. \end{aligned} \tag{2.26}$$

Thus, the approximate spatial extent of the kernel can be deduced from the cut-off frequencies. Therefore, the discrete impulse response $h_{zD}(n,m)$ given by,

$$h_{zD}(n,m) = \begin{cases} h_z(Xn,Ym) & |n| \le \dfrac{N_h-1}{2}\ ,\ |m| \le \dfrac{M_h-1}{2} \\ 0 & \textit{else} \end{cases} \tag{2.27}$$

characterizes the discrete linear system. N_h and M_h are odd integers and they give the discrete size of the filter in dimensions n and m, respectively. They are defined as,

$$N_h = 2[\![\frac{|x_c|}{X}]\!] + 1 \ ,$$
$$M_h = 2[\![\frac{|y_c|}{Y}]\!] + 1 \ , \tag{2.28}$$

where, X and Y are the sampling periods in x and y coordinates, respectively. (If an even length filter is desired, then the domain of eq.(2.27) can be changed to $n \in [\frac{-N_h}{2} + 1, \frac{N_h}{2}]$, and $m \in [\frac{-M_h}{2} + 1, \frac{N_h}{2}]$.) Similarly, the input function can be discretized to yield,

$$a_D(n,m) = a(Xn,Ym) \ . \tag{2.29}$$

If the size of $a_D(n,m)$ is $N_a \times M_a$, then the discrete field $\psi_{zD}(n,m)$ can be found as discrete linear convolution of two finite size two-dimensional sequences, $a_D(n,m)$ and $h_{zD}(n,m)$. There are many well known efficient methods to do this task [38-40]. The resultant discrete field has the size $(N_h + N_a - 1) \times (M_h + M_a - 1)$. The final "magnitude square" operation to get the intensity is trivial.

In order to increase computational efficiency, circular convolution can be used instead of linear convolution, i.e.,

$$\psi_{zD}(n,m) = \left[1 - a_D(n,m)\right] \circledast\circledast h_{zD}(n,m) \ . \tag{2.30}$$

The implicit periodicity assumption of using circular convolution affects the results in the form of overlapping and wrapping. If the size of the convolution is not large enough to

cover the size of the resultant field $\psi_{zD}(n,m)$, as given above, then overlapping occurs. This phenomenon affects the accuracy of simulations, and is more detrimental to the reconstructions since the size of the reconstructed field is significantly larger than that of recording (the size is $(N_a + 2N_h - 2)\times(M_a + 2M_h - 2)$). This size expansion in the reconstruction occurs only for the twin-image component (and also for some of the non-linear terms) but not for the desired reconstructed object. Therefore, the effect is not significant if the purpose is to reconstruct the object distribution. However, if the simulation is done, for instance, to check the twin-image effect, then necessary precautions must be taken, as explained above, to have a faithful simulation.

Discrete simulations based on the discretized version of the continuous model of Fig.4 (Type I) using circular convolution are done using the formulation given below.

The continuous Fourier transform of the convolution kernel $h_z(x,y)$ is known analytically as,

$$H_z(u,v) = \mathcal{F}\left\{h_z(x,y)\right\} = \mathcal{F}\left\{\frac{1}{j\lambda z}\exp\left[j\frac{\pi}{\lambda z}(x^2+y^2)\right]\right\} = \exp\left[-j\frac{\lambda z}{4\pi}(u^2+v^2)\right]. \qquad (2.31)$$

The band-limited version is used for the simulations. Therefore,

$$H_{zLP}(u,v) = \begin{cases} \exp\left[-j\frac{\lambda z}{4\pi}(u^2+v^2)\right] & |u| \le u_c \text{ and } |v| \le v_c \\ 0 & else \end{cases}, \qquad (2.32)$$

$H_{zLP}(u,v)$ is sampled to get the discrete version:

$$H_{zD}(k,l) = H_{zLP}(Uk,Vl) \ , \tag{2.33}$$

where, U and V are the sampling periods in coordinates u and v, respectively. It is shown in section 2.3.1 that $h_{zLP}(x,y)$ is almost space-limited. In order not to have overlapping in (x,y) domain (the size of the object is assumed to be negligible compared to the size of the kernel), it is necessary to have (also see eq.(2.26)),

$$\begin{aligned} \frac{\pi}{U} &\geq x_c = \frac{\lambda z}{2\pi} u_c \ , \\ \frac{\pi}{V} &\geq y_c = \frac{\lambda z}{2\pi} v_c \ . \end{aligned} \tag{2.34}$$

(If the size of the object is not negligible, then x_c and y_c in eq.(2.24) above, must be replaced by $x_c + \frac{N_a X}{2}$ and $y_c + \frac{M_a Y}{2}$.) Suppose that the size of circular convolution is $N \times M$. In order to utilize the complete range $N \times M$, to represent $H_{zD}(k,l)$, the sampling rate must satisfy,

$$\begin{aligned} U\frac{N}{2} &= u_c \ , \\ V\frac{N}{2} &= v_c \ . \end{aligned} \tag{2.35}$$

Combining eq.(2.34) and eq.(2.35) yields,

$$\frac{\pi}{U} \geq \frac{\lambda z}{2\pi} U \frac{N}{2} \quad ,$$

$$\frac{\pi}{V} \geq \frac{\lambda z}{2\pi} V \frac{N}{2} \quad , \tag{2.36}$$

which results in,

$$U \leq \frac{2\pi}{(\lambda z N)^{1/2}} \quad ,$$

$$V \leq \frac{2\pi}{(\lambda z N)^{1/2}} \quad . \tag{2.37}$$

Furthermore, if the sampling in (x,y) domain is carried out to have exactly N samples per period in x coordinate (period $= 2\pi/U$), and exactly M samples per period in y coordinate, (period $= 2\pi/V$), then,

$$XN = \frac{2\pi}{U} \quad ,$$

$$YM = \frac{2\pi}{V} \quad . \tag{2.38}$$

In order to utilize the complete region $N \times M$, also in (x,y) domain, the inequalities in the equations above must be converted to equalities. In this case, from eq.(2.37) and eq.(2.38),

$$X = \left[\frac{\lambda z}{N}\right]^{1/2} \quad ,$$

$$Y = \left[\frac{\lambda z}{M}\right]^{1/2} \quad . \tag{2.39}$$

In practice it is very hard to achieve such precision, but it is not necessary to do so since slight overlappings (larger sampling period in u,v domain), or slight waste in the usable region (smaller sampling period in the u,v domain) in the x,y domain is acceptable.

In order to efficiently compute the circular convolution (see Fig.7), the discrete Fourier transform of the $N \times M$ input object is taken. Because of the restrictions imposed by the fast Fourier transform algorithm used, the size of the circular convolution is restricted to be $N = 2^r$, and $M = 2^s$, where r and s are positive integers. The symmetrical discrete kernel $H_{zD}(k,l)$, which is zero for $k \notin \left[-\frac{N}{2}+1, \frac{N}{2}\right]$ or $l \notin \left[-\frac{M}{2}+1, \frac{M}{2}\right]$, is periodically extended by duplicating it beyond that region. The $N \times M$ portion of this periodic signal corresponding to $k \in [0, N-1]$ and $l \in [0, M-1]$, is multiplied by size $N \times M$ discrete Fourier transform of the input. Finally, an inverse discrete Fourier transform is taken to get the periodic field $\psi_{zD}(n,m)$. A point-by-point magnitude square operation gives the desired result $I_{zD}(n,m)$, which is the hologram.

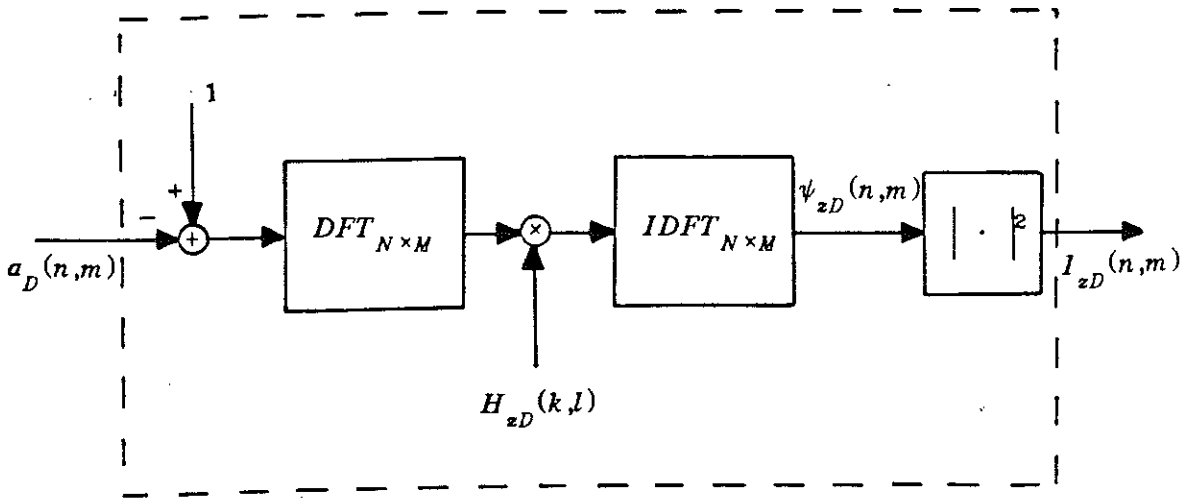

Figure 7. The discrete implementation of the continuous system given in Fig.4.

The conclusion on the digital simulations using circular convolutions can be summarized as follows: the noise-free (assuming that the digitization is negligible) hologram of a periodic two-dimensional object, whose each period is an exact replica of the displayed $N \times M$ image, is generated, resulting in a periodic hologram; one period of it is displayed. (This statement is correct whether there is overlapping or not.) (See Fig.8.)

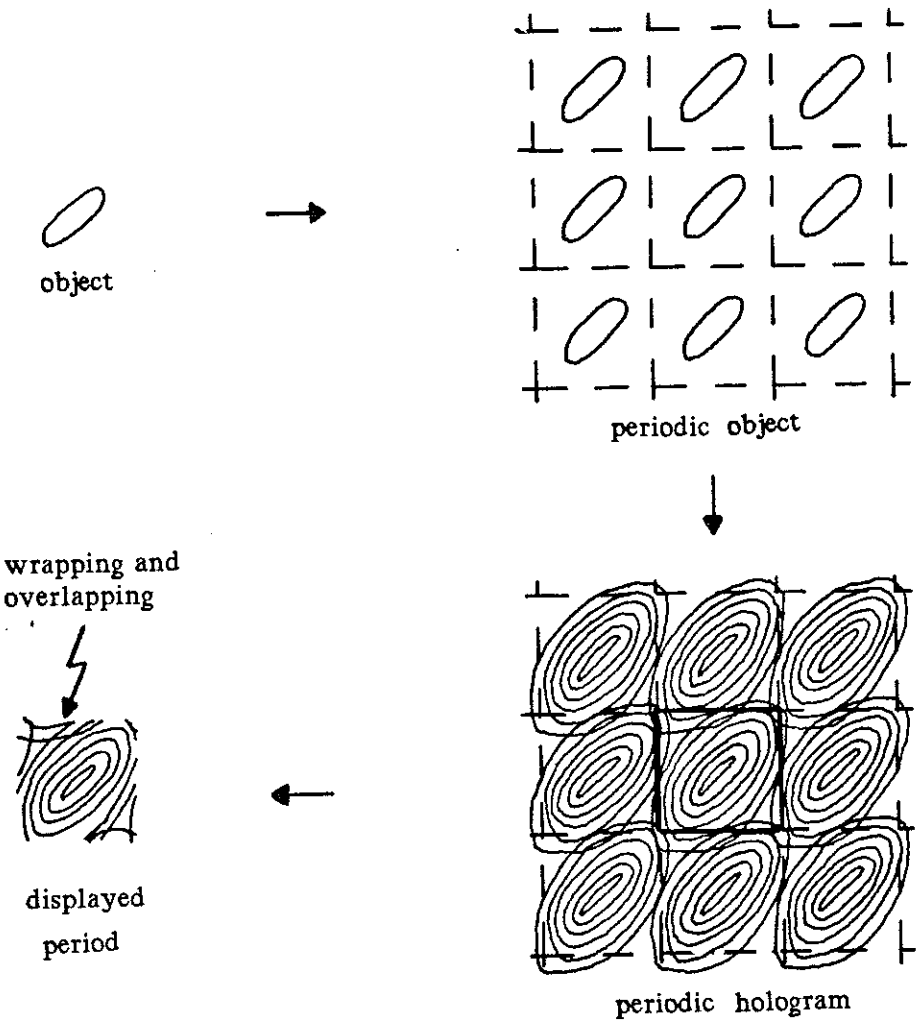

Figure 8. The effect of implicit periodicity.

2.3.2.1. Results The simulation results (Type I) given below are implemented following the formulation above (See Fig.7). The same sampling periods are used for x and y coordinates. Therefore,

$$X = Y \quad \text{and} \quad U = V \ . \tag{2.40}$$

Also a square two-dimensional circular convolution size of 512×512 is selected. The circular convolution is efficiently implemented using a two-dimensional fast Fourier transform algorithm. For the purpose of normalization, a new variable α is introduced, such that,

$$\alpha^2 \frac{\pi}{N} = \frac{\pi}{\lambda Z} X^2 \ . \tag{2.41}$$

Therefore, the equality condition of eq.(2.34) is equivalent to $\alpha = 1$. If the simulation of the reconstruction stage of an actual optical hologram is done, then the sampling of the optical hologram is adjusted to have α close to 1, using eq.(2.41). Note that the parameter α is the only parameter which characterizes the overall hologram system, within a gain factor, once the size is set as constant $N \times N$, since,

$$h_{zD} = K \exp\left[j \frac{\pi}{\lambda Z} X^2 (n^2 + m^2) \right] = K \exp\left[\alpha^2 \frac{\pi}{N} (n^2 + m^2) \right] \ . \tag{2.42}$$

The parameter α also uniquely defines $H_{zD}(k,l)$: from eq.(2.41) and eq.(2.38), we can write,

$$\frac{1}{\alpha^2} = \frac{\lambda z}{4\pi^2} N U^2 \ . \tag{2.43}$$

So,

$$\frac{1}{\alpha^2}\frac{\pi}{N} = \frac{\lambda z}{4\pi} U^2 \ . \tag{2.44}$$

Therefore $H_{zD}(k,l)$ can be written as,

$$H_{zD}(k,l) = \exp\left[-j\frac{\lambda z}{4\pi} U^2 (k^2+l^2)\right] = \exp\left[-j\frac{1}{\alpha^2}\frac{\pi}{N}(k^2+l^2)\right] \ . \tag{2.45}$$

The synthesized images displayed below are obtained using a COMTAL Vision One/20 image processing system. Each has 512 × 512 pixels, and each pixel has 256 gray levels. An image whose hologram is to be simulated is transferred to a VAX/11 mini-computer. The computations are performed using real arithmetic for accuracy, by executing the subroutine given in Appendix A. The results of the computations are converted to 256 gray level images. For most of the pictures, this is done by assigning the lowest pixel value to 0, and the highest one to 255. This assures the maximum use of the dynamic range of the gray scale, but the DC level shift and the gain used to achieve this result are different for each image. The resultant images are transferred back to the image processing system for display. For all synthesized objects, white (gray level 255) corresponds to total transparency, whereas black (gray level 0) represents completely opaque areas.

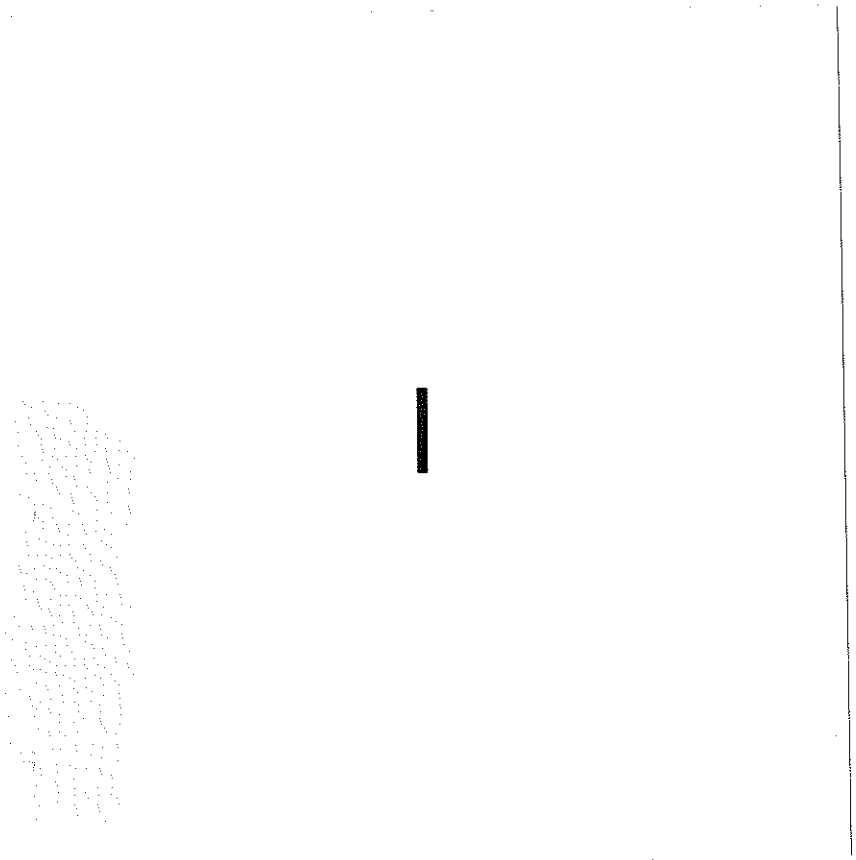

Figure 9. A synthesized object.

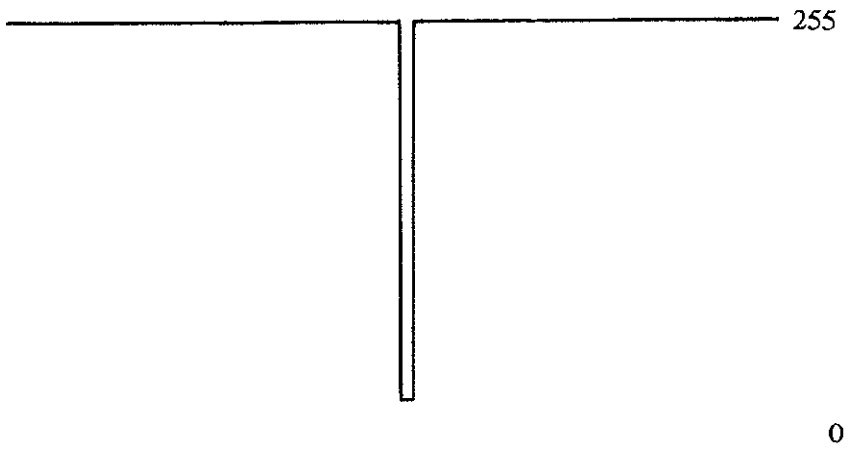

Figure 10. Profile of the object of Fig.9 through center.

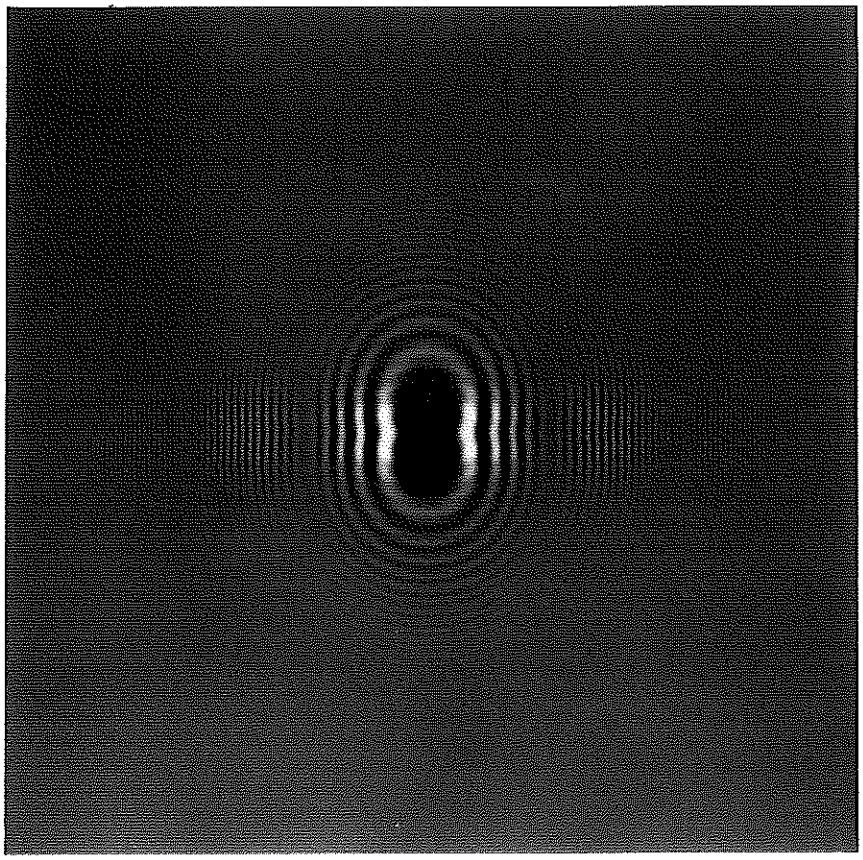

Figure 11. The simulated in-line Fresnel hologram (Type I) of object shown in Fig.9. $\alpha = 1$.

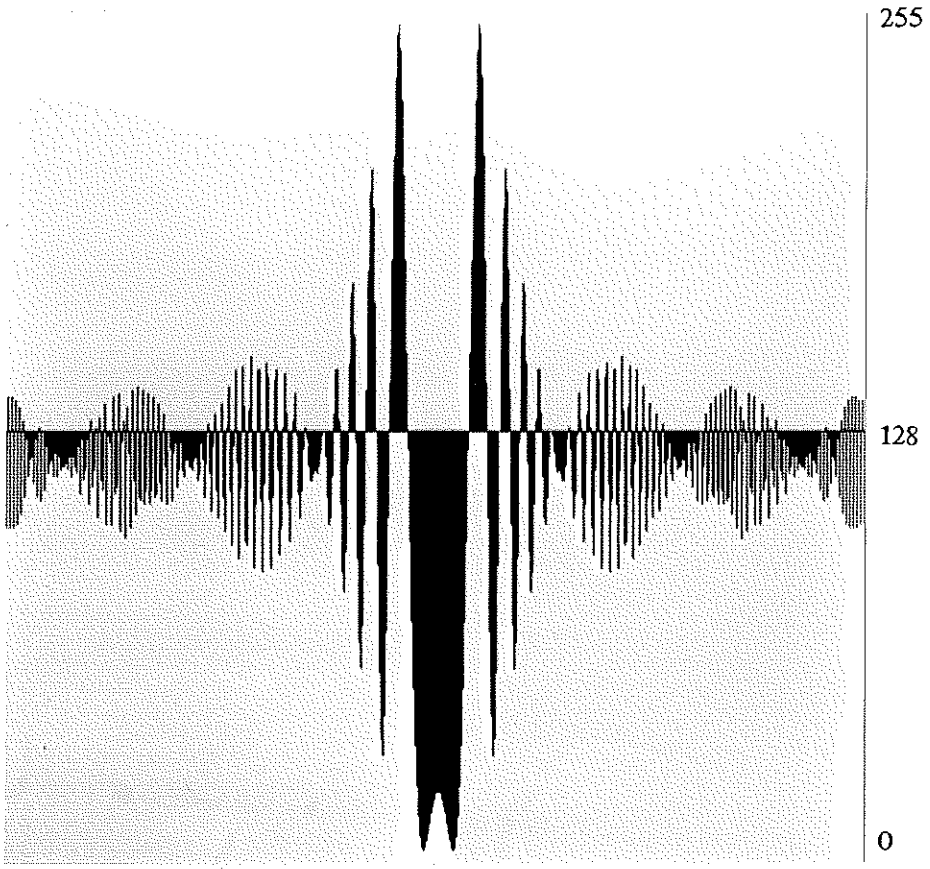

Figure 12. Profile[2] of the hologram of Fig.11 through center.

[2] Profiles given in this dissertation are graphic representations of gray levels on a cross-sectional line of an image. The graphs are on white background, and for visual convenience, the area between the graph and the center gray level (128) is filled with black.

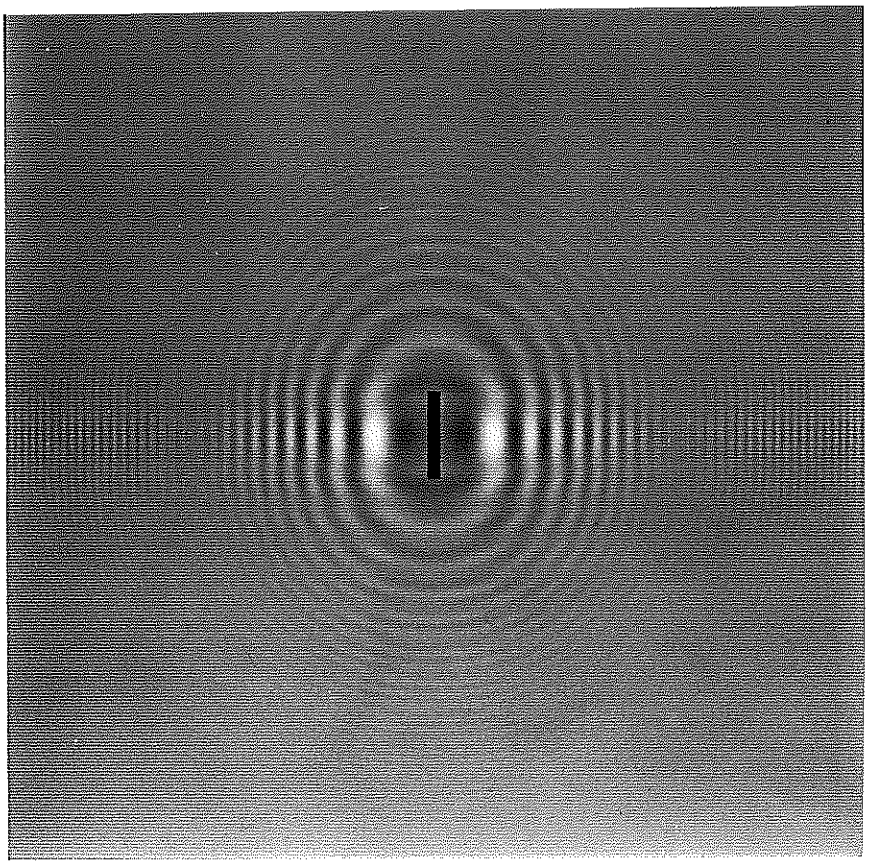

Figure 13. Digital reconstruction (Type I) from the hologram of Fig.11.

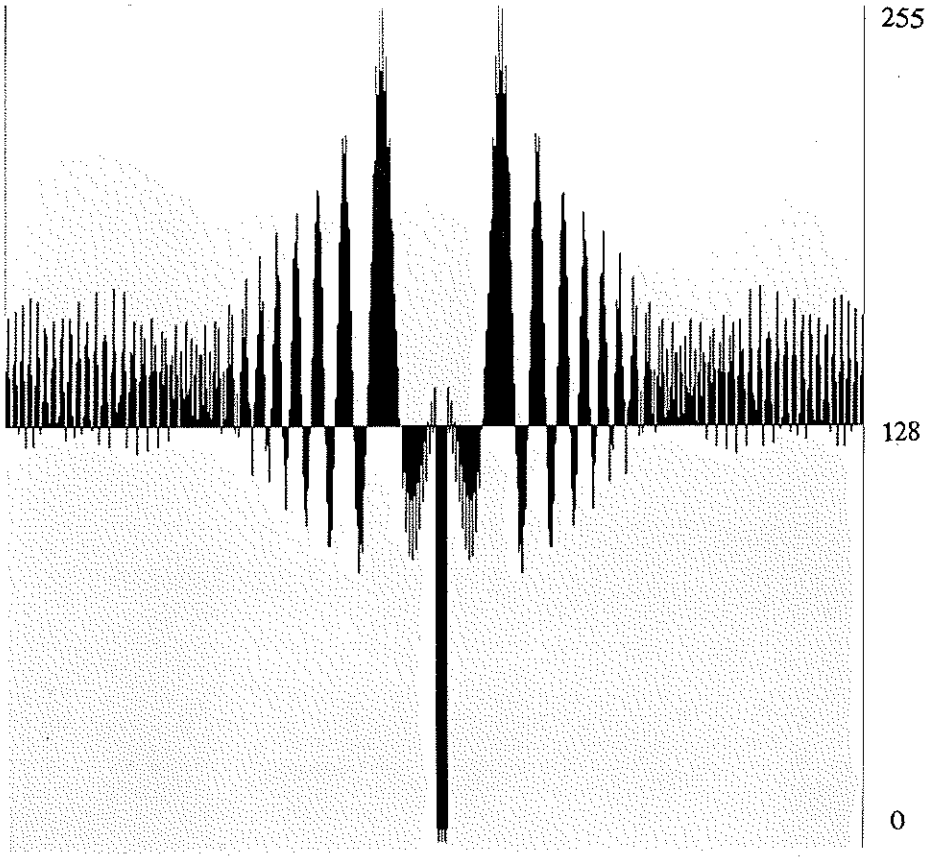

Figure 14. The profile of reconstruction of Fig.13 through center.

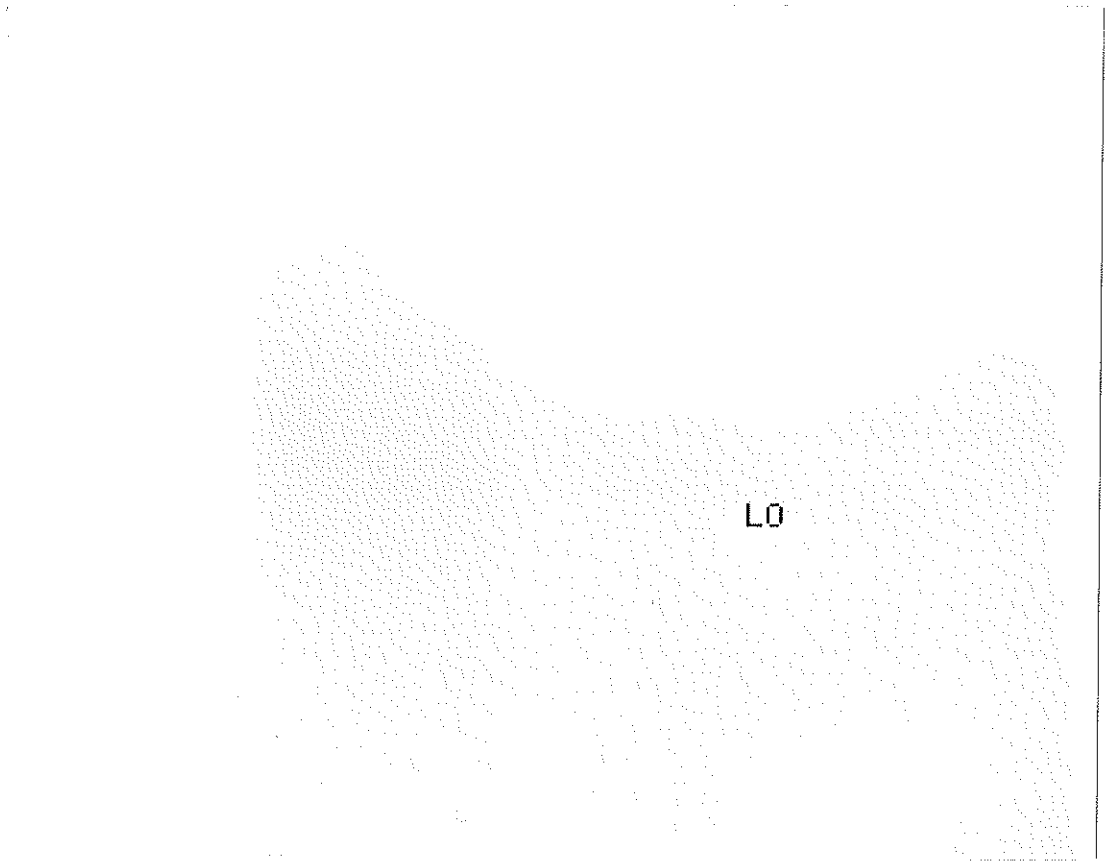

Figure 15. Another synthesized object.

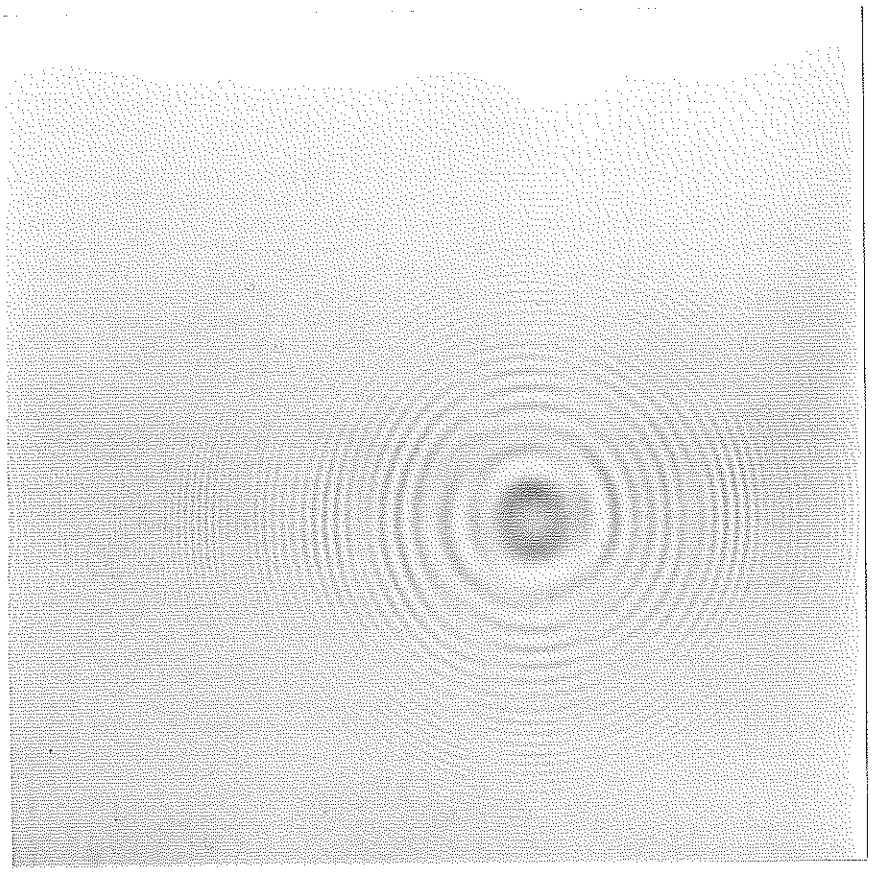

Figure 16. Simulated in-line Fresnel hologram (Type 1) of object shown in Fig.15. $\alpha = 0.8$.

Since the object is very small compared to circular convolution size this hologram is a typical far-field hologram.

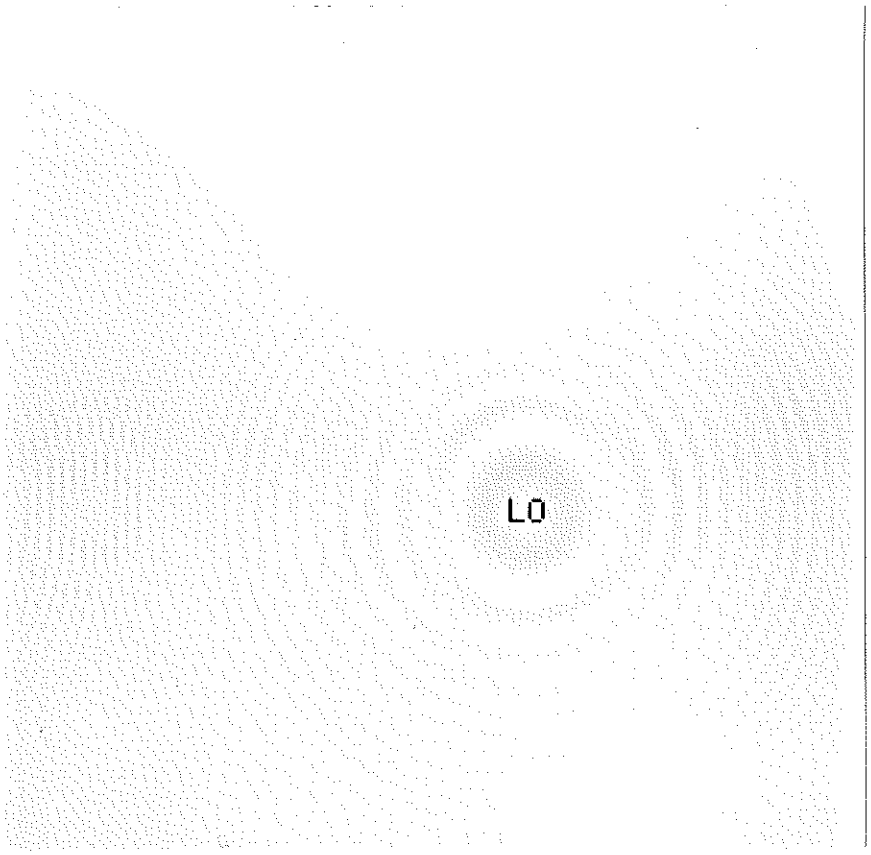

Figure 17. Digital reconstruction (Type I) from the hologram shown in Fig.16.

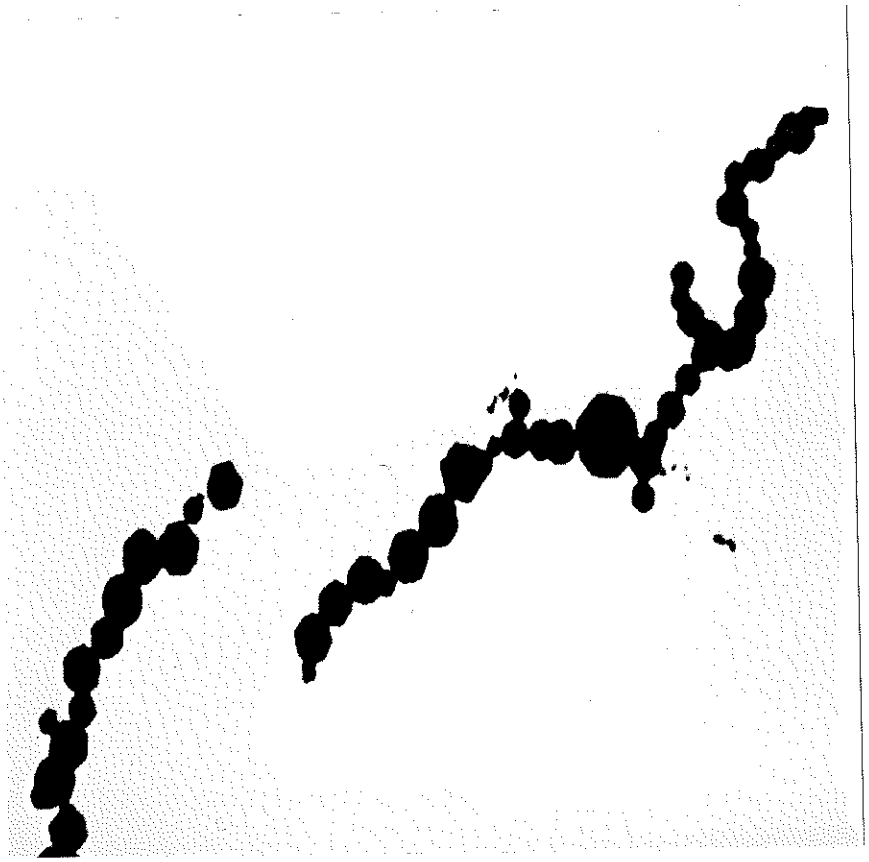

Figure 18. Another simulated object.

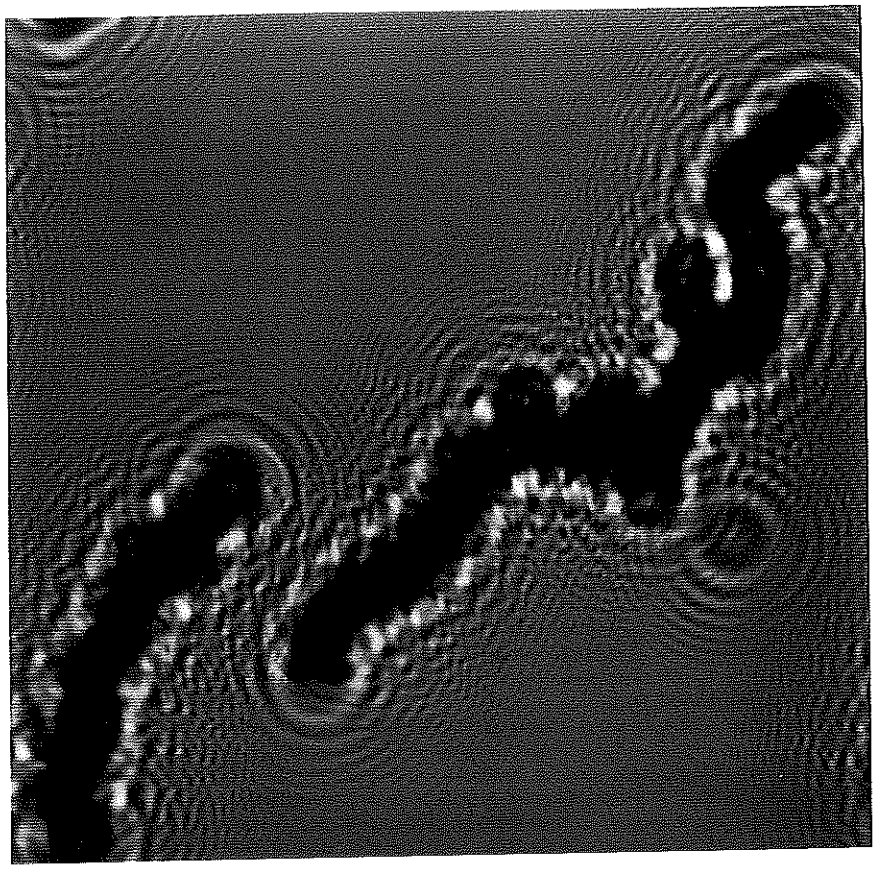

Figure 19. Simulated in-line Fresnel hologram of object shown in Fig.18. $\alpha = 1.05$.

Note that the object size is almost same as the circular convolution size. Therefore, overlapping effect is significant.

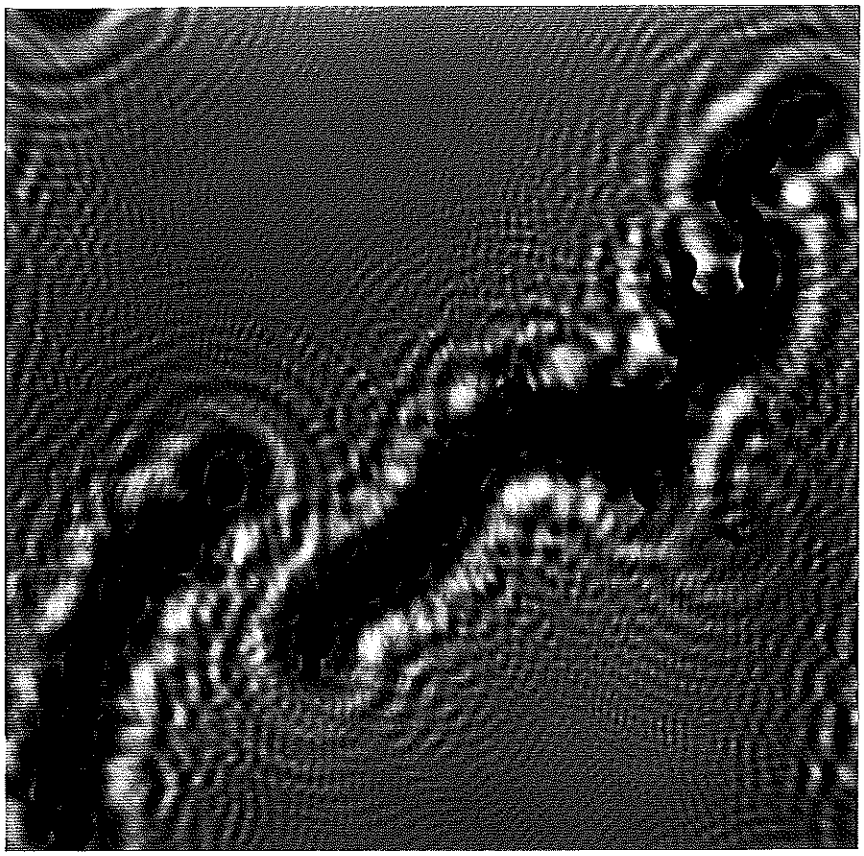

Figure 20. Digital reconstruction (Type I) from the hologram shown in Fig.19.

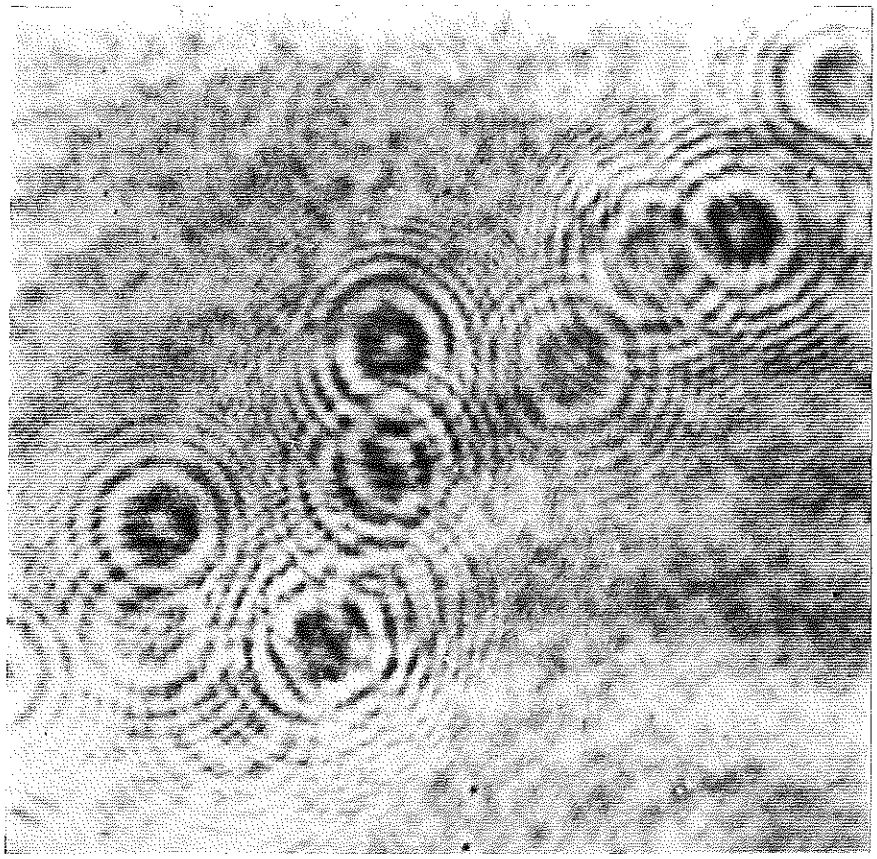

Figure 21. A digitized optical hologram.

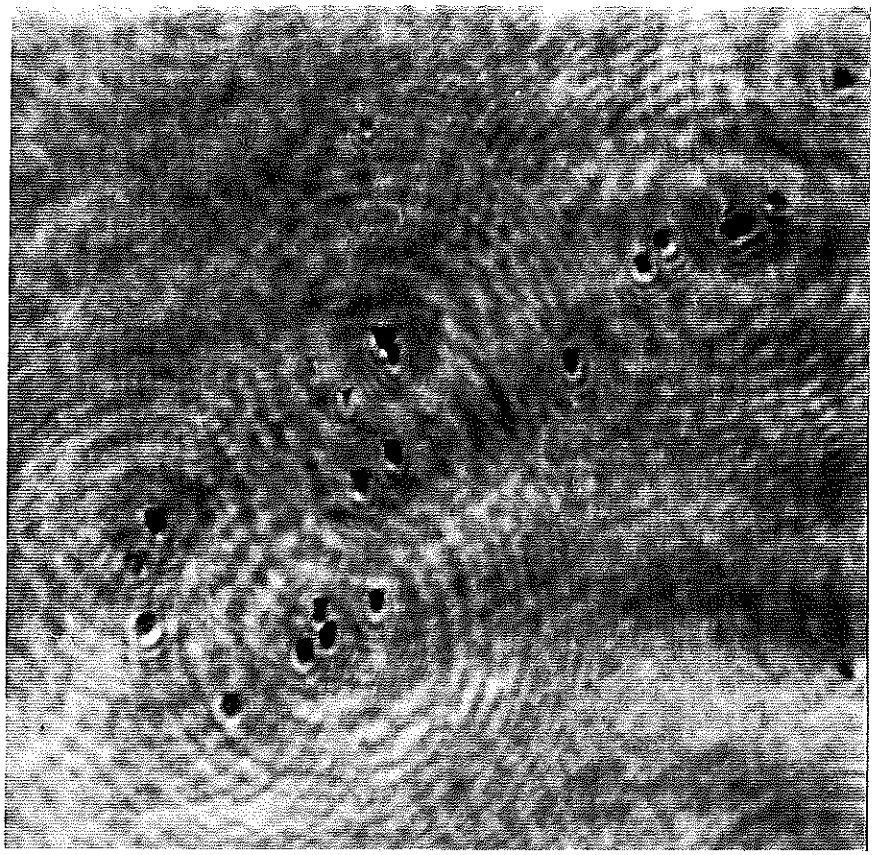

Figure 22. Digital reconstruction from the hologram of Fig.21. $\alpha = 0.962$.

2.3.3. Digital simulation of in-line holography (Type II)

The digital simulation based on the system model of Fig.5 is called Type II. The formulation for the continuous case is given in eq.(2.9) as,

$$I_z(x,y)=\frac{1}{(\lambda z)^2}\left|\int_{-\infty}^{\infty}\int_{-\infty}^{\infty}\left[1-a(\xi,\eta)\right]\exp\left[j\frac{\pi}{\lambda z}(\xi^2+\eta^2)\right]\exp\left[-j\frac{2\pi}{\lambda z}(\xi x+\eta y)\right]\,d\xi d\eta\right|^2, \quad (2.46)$$

Suppose that the variables ξ and η are discretized using sampling periods P and Q, respectively. Also suppose that the variables x and y are sampled with periods X and Y. Let the input function $\left[1-a(\xi,\eta)\right]$ be space limited, such that it equals zero for $\xi \notin [\,0\,,(N-1)P\,]$ or $\eta \notin [\,0\,,(M-1)Q\,]$. In this case, eq.(2.46) can be written in discrete domain as,

$$\begin{aligned} I_{zD}(n,m) &= I_z(nX,mY) = \\ &= \frac{1}{(\lambda z)^2}\left|\sum_{p=0}^{N-1}\sum_{q=0}^{M-1}\left[1-a(pP,qQ)\right]\exp\left[j\frac{\pi}{\lambda z}(P^2p^2+Q^2q^2)\right]\right. \\ &\qquad \left.\exp\left[-j\frac{2\pi}{\lambda z}(PXpn+QYqn)\right]\right|^2. \end{aligned} \quad (2.47)$$

If the sampling periods X, Y, P and Q are chosen to satisfy,

$$\frac{2\pi}{\lambda z} XP = \frac{2\pi}{N} ,$$
$$\frac{2\pi}{\lambda z} YQ = \frac{2\pi}{M} , \qquad (2.48)$$

then eq.(2.47) can be written as,

$$I_{zD}(n,m) =$$
$$\frac{1}{(\lambda z)^2}\left|\sum_{p=0}^{N-1}\sum_{q=0}^{M-1}\left[1-a_D(p,q)\right]\exp\left[j\frac{\pi}{\lambda z}(P^2p^2+Q^2q^2)\right]\exp\left[-j(\frac{2\pi}{N}np+\frac{2\pi}{M}mq)\right]\right|^2. \qquad (2.49)$$

From eq.(2.49) and from the definition of discrete Fourier transform, the equation above becomes,

$$I_{zD}(n,m) = \frac{1}{(\lambda z)^2}\left| DFT\left\{\left[1-a_D(p,q)\right]\exp\left[\frac{\pi}{\lambda z}(P^2p^2+Q^2q^2)\right]\right\}\right|^2 . \qquad (2.50)$$

Note that both variable sets n,m and p,q correspond to space variables, for hologram and input object, respectively, even though they are related by a discrete Fourier transform.

As in Type I, Type II simulation also implies periodicity through the discrete Fourier transform used. However, there is a delicate conceptual difference between the periodicity of the two cases: the periodicity of Type I is induced by circular convolution, whereas the periodicity of Type II is the outcome of a single discrete Fourier transform. In order to show the nature of periodicity in Type II, suppose there is an illuminated (space limited illumination) continuous domain object distribution, as indicated above. (This is equivalent

to saying that there is a window just in front of the object distribution which passes the light in a limited space, but blocks the rest.) The continuous hologram obtained from this space limited illumination has a strong edge effects as a result of the sharp boundary which limits the illumination. Now, suppose that the illuminated object distribution $\left[1-a(\xi,\eta)\right]$ is discretized by sampling. Since the hologram field is given by a Fourier transform relationship, the effect of discretization in (ξ,η) domain results in shifting-and-adding in (x,y) domain. Depending on the sampling rate, the separation of the shifts will be different. If the sampling rate in (ξ,η) domain is too high, then the individual holograms with strong edge effects will not overlap. Otherwise, there will be overlapping. Analytically, sampling in (ξ,η) domain with sampling periods P and Q, respectively, results in a continuous periodic hologram in (x,y) domain, as:

$$\tilde{I}_z(x,y) = \sum_{r=-\infty}^{\infty}\sum_{s=-\infty}^{\infty} I_z(x-\frac{\lambda z}{P}r, y-\frac{\lambda z}{Q}s), \tag{2.51}$$

where $I_z(x,y)$ has the edge-effect as indicated above. Similarly, sampling of $\tilde{I}_z(x,y)$ implies the assumption that the input object distribution is also periodic, where the periodicity is induced by shifting-and-adding, i.e, if,

$$f(\xi,\eta) = \begin{cases} \left[1-a(\xi,\eta)\right] & \xi \le |\frac{PN}{2}, \text{ and } \eta \le \frac{QM}{2} \\ 0 & else \end{cases}, \tag{2.52}$$

then the periodic input will be,

$$\tilde{f}(\xi,\eta) = \sum_{r=-\infty}^{\infty}\sum_{s=-\infty}^{\infty} f(\xi-\frac{\lambda z}{X}r,\eta-\frac{\lambda z}{Y}s) \tag{2.53}$$

Note that from eq.(2.48), the periods in (ξ,η) domain, $\frac{\lambda z}{X}$, and $\frac{\lambda z}{Y}$ are found as,

$$\begin{aligned} \frac{\lambda z}{X} &= PN \ , \\ \frac{\lambda z}{Y} &= QM \ , \end{aligned} \tag{2.54}$$

which is the expected result of using the discrete Fourier transform for an $N \times M$ sequence, where the sequence is obtained from a continuous function with sampling periods P and Q. Once, the sampling periods in the (ξ,η) domain are fixed, then the sampling periods in the (x,y) domain are also fixed from eq.(2.54). Note that the corresponding periods in the two domains are not necessarily equal. Therefore, the spatial extents of one period in two continuous domains are different. So, in the hologram domain, it is possible to get results beyond the illuminated region if one period is larger than the size of the illumination. In this case, the portion of the result lying out of the region is the edge effect oscillations around zero level, with overlapping from other periods. On the other hand, if the period is smaller than the object illumination size, then overlapping of holograms from adjacent periods occurs. The first case corresponds to

$$\begin{aligned} P &< \left[\frac{\lambda z}{N}\right]^{1/2} \ , \\ Q &< \left[\frac{\lambda z}{M}\right]^{1/2} \ , \end{aligned} \tag{2.55}$$

and the conditions for the second case can be obtained by changing the direction of inequalities above. The equality case of eq.(2.55) is interesting. In this case, the corresponding sampling rates in the two domains are equal, i.e., $X = P$ and $Y = Q$. Also in this case, the overlapping of the edge effects occurs such that the edge-effect components from adjacent periods cancel each other. The formulations of Type I and Type II are exactly equivalent only in this case. To show this, first a coefficient, β, is defined similar to α, i.e.,

$$\begin{aligned} \beta^2 \frac{\pi}{M} &= \frac{\pi}{\lambda z} Q^2 \ , \\ \alpha^2 \frac{\pi}{N} &= \frac{\pi}{\lambda z} P^2 \ . \end{aligned} \tag{2.56}$$

The conditions,

$$\begin{aligned} X = P &= \left[\frac{\lambda z}{N}\right]^{1/2} \ , \\ Y = Q &= \left[\frac{\lambda z}{M}\right]^{1/2} \ , \end{aligned} \tag{2.57}$$

are equivalent to have $\alpha = 1$ and $\beta = 1$. In this case, the discrete normalized periodic kernel becomes (gain factor is ignored),

$$h_D(n,m) = \exp\left[j\left(\frac{\pi}{N} n^2 + \frac{\pi}{M} m^2\right)\right] \ . \tag{2.58}$$

So, Type I formulation (see eq.(2.30)) can be written as (see eq.(2.58),

$$I(n,m) = \left| \sum_{p=0}^{N-1} \sum_{q=0}^{M-1} \left[1-a_D(p,q)\right] \exp\left[j\left(\frac{\pi}{N}(n-p)^2 + \frac{\pi}{M}(m-q)^2\right)\right] \right|^2 . \qquad (2.59)$$

Expanding the quadratic exponents as in eq.(2.8), we get,

$$I(n,m) = \left| \exp\left[\frac{\pi}{N}n^2 + \frac{\pi}{M}m^2\right)\right| \sum_{p=0}^{N-1} \sum_{q=0}^{M-1} \left[1-a_D(p,q)\right] \exp\left[j\left(\frac{\pi}{N}p^2 + \frac{\pi}{M}q^2\right)\right] \exp\left[-j\left(\frac{2\pi}{N}pn + \frac{2\pi}{M}qm\right)\right] \Bigg|^2 , \qquad (2.60)$$

which can be reduced to,

$$I(n,q) = \left| \sum_{p=0}^{N-1} \sum_{q=0}^{M-1} \left[1-a_D(p,q)\right] \exp\left[j\left(\frac{\pi}{N}p^2 + \frac{\pi}{M}q^2\right)\right] \exp\left[-j\left(\frac{2\pi}{N}pn + \frac{2\pi}{M}qm\right)\right] \right|^2 , \qquad (2.61)$$

where it is equal to the formula for Type II simulation:

$$I(n,m) = \left| DFT\left\{ \left[1-a_D(p,q)\right] \exp\left[j\left(\frac{\pi}{N}p^2 + \frac{\pi}{M}q^2\right)\right] \right\} \right|^2 . \qquad (2.62)$$

The Type II simulation can be summarized as follows: periodically shifted overlappings of the hologram of a two-dimensional object distribution which is illuminated by a finite-extent illumination (window) is generated, and its one period is

displayed. Type I and Type II simulations are exactly equivalent only if some certain conditions are met related to sampling.

A final remark is about the computational complexity of the Type II simulations. The amount of computation required for a Type II simulation is the same as that of the far-field case (see eq.(2.16)) since both of them, require a single DFT computation together with a single array multiplication and a final magnitude squaring. Therefore, computing the more accurate Fresnel hologram requires the same computational effort as computing the far-field hologram. Even in Type I simulations, the difference of computational requirement of Fresnel simulations compared to the far-field case is an additional discrete Fourier transform. The extra computational effort is justified, however, not only by the increased accuracy, but also because of the enourmous additional range of possible simulations that can be performed.

2.3.3.1. Results The simulation results (Type II) given below are implemented following the formulation above. The same sampling periods are used for ξ and η coordinates so that,

$$P = Q \quad \text{and} \quad X = Y \ . \tag{2.63}$$

An object size of 512 × 512 is used throughout the simulations shown. The discrete Fourier transform is efficiently implemented using the same two-dimensional fast Fourier transform algorithm as in Type I simulations. Note that, computationally, Type II simulations are significantly more efficient compared to Type I, since one fast Fourier transform operation is completely eliminated. But, if the parameter α is not equal to 1, then there is strong edge-effect in Type II. Furthermore, if $\alpha \neq 1$, then the sampling periods in the two space domains corresponding to the input object and the hologram are different in Type II. (They are always equal in Type I.) During display, one sample corresponds to one

pixel which has a certain fixed size. Therefore, even though the physical sampling periods are different in two domains, they are displayed as if they were same. The result is a change in the scale for the input object and the hologram. If $\alpha < 1$, then the sampling period X, is larger than P. So, the image in (x,y) domain will look smaller when displayed. The scale is proportional to α.

Therefore, if the simulation of hologram recording is to be done, α can be set to be 1, and in this case Type II simulator must be preferred to Type I since they both generate the same result and since Type II is much more efficient computationally. For digital reconstructions from optical holograms, α can not be made exactly one, therefore it is better to use Type I simulator to avoid scale change and strong edge-effects (The edge-effect in Type I is only due to mismatch of the gray levels at parallel edges of the hologram portion, which is not significant in most of the cases.) It is possible to decrease the edge-effect by using a window which softens the sharp edges of the input object, but it is not done in the results shown to emphasize the difference of the two simulations.

The following images show some applications of Type II simulator. The synthesized objects are generated using a COMTAL Vision One/20 image processing system, and as in Type I, each has 512×512 pixels, and each pixel has 256 gray levels. A VAX/11 mini-computer receives the image from the processor, and generates the result by executing the subroutine given in Appendix B. The computations are done using real arithmetic, but the output is converted to 256 gray levels, as in Type I case, for display at the image processor.

Figure 23. A synthesized object.

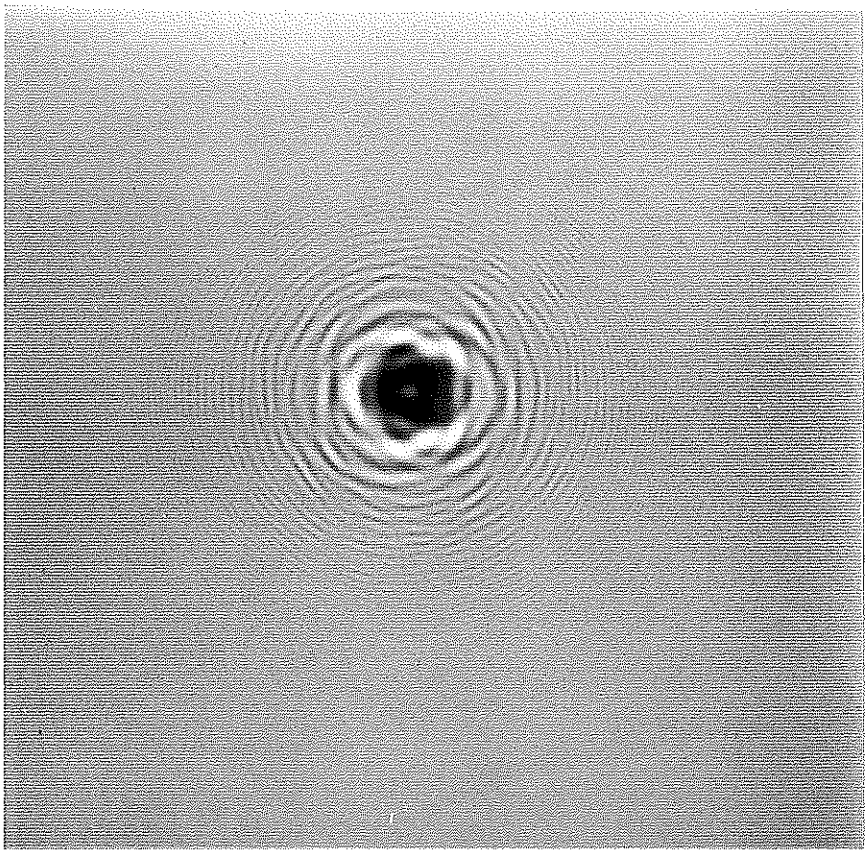

Figure 24. Simulated hologram (Type II) of the object shown in Fig.23. ($\alpha=1$).

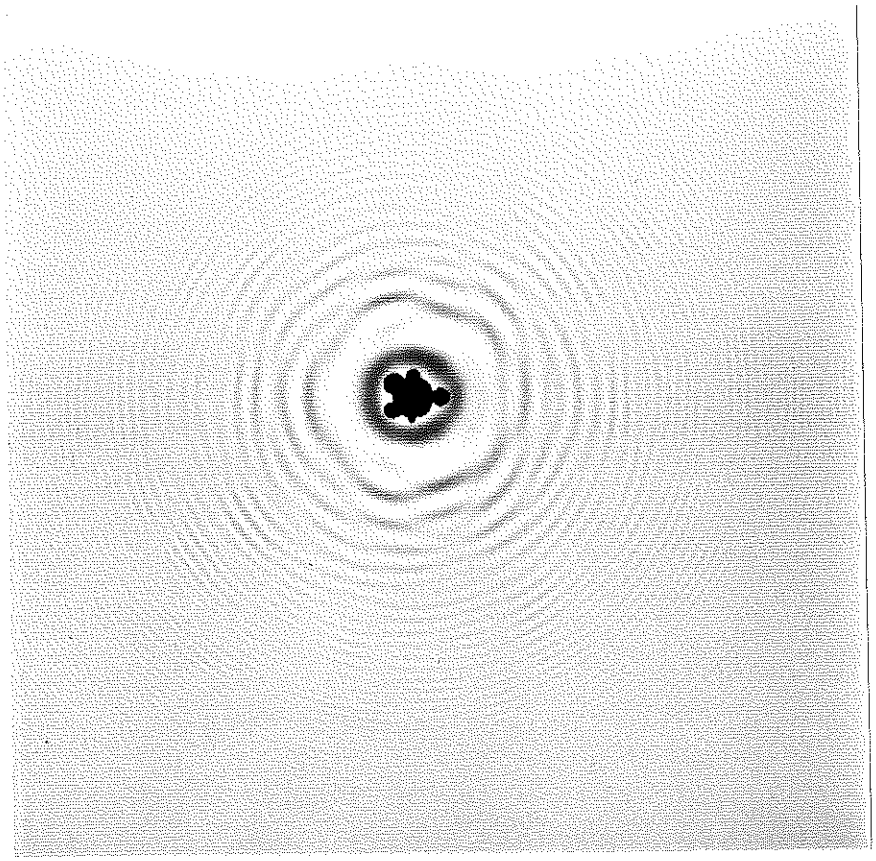

Figure 25. Digital reconstruction (Type II) from the hologram of Fig.24.

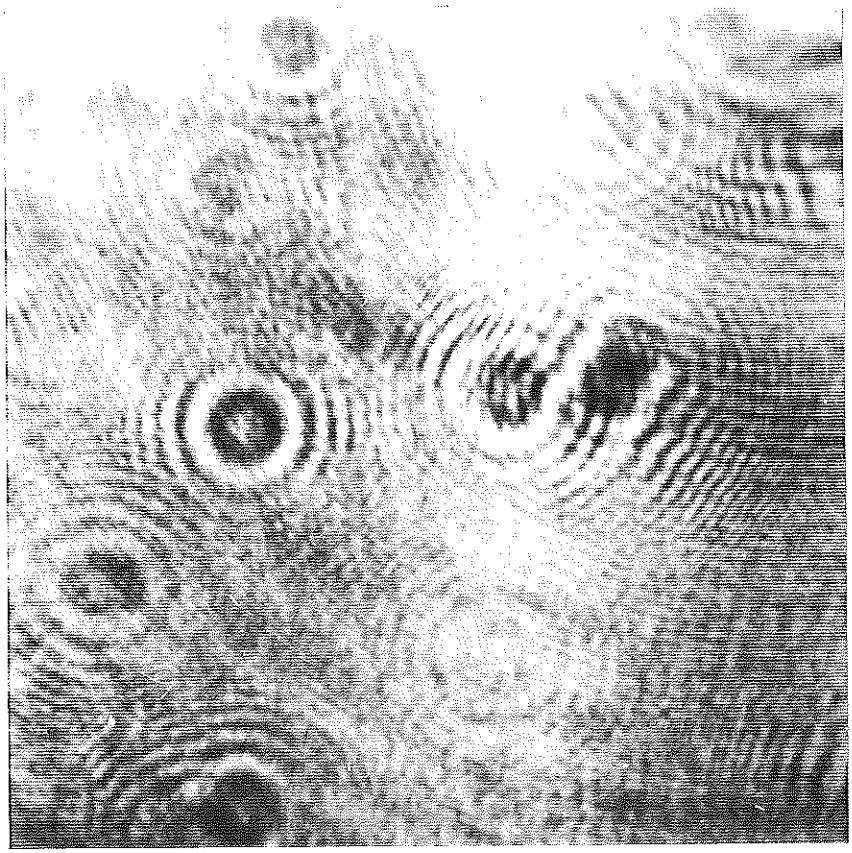

Figure 26. A digitized optical hologram.

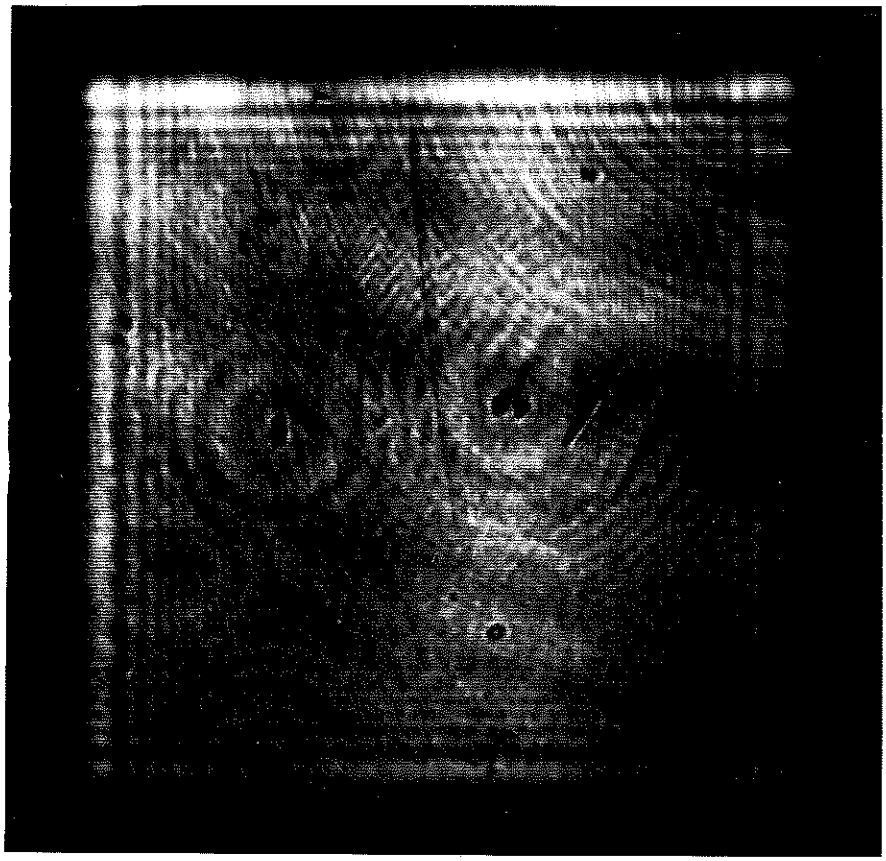

Figure 27. Digital reconstruction (Type II) from the hologram shown in Fig.26. $\alpha = 0.930$.

Note that the scale is different in the hologram and the reconstruction as indicated in the text. Also, the edge-effect is clearly visible.

2.4. Comparison of Digital Reconstructions with Optical Reconstructions

The optical recording and reconstruction form a two-step process, where the same process of recording is repeated for reconstruction. Every physical process inevitably adds distortion, mainly for two reasons: system imperfections and random noise. System imperfections arise either because of the imperfect components (such as lenses, coherence of laser, quality of recording film in optical holography) or because of the very nature of the process which does not match the mathematical model given. For instance, in in-line holography, the optical retrieval of the object distribution is solely based on the nice property of the mathematical model as given in eq.(2.10.a). However, the model is based on approximations, and nature does not work exactly as the model. Therefore, the optical recording process deviates from the ideal case, and a subsequent optical recording makes the deviation worse.

On the other hand, in the simulations given in previous chapters, where both the hologram and the reconstruction of synthesized objects are simulated, the overall digital process follows the strict mathematical formulation that the simulations are based on. In this case, it is known beforehand that the discrete version of eq.(2.10.a) holds. Therefore, the object component of the reconstructions are exactly the same as the original object.

In the case of optical recording and digital reconstruction, the overall process still deviates from the ideal case, but since the imperfect second stage (reconstruction) is replaced by an ideal computational one (assuming digitization effects are negligible), the overall system is more close to the ideal case than the pure optical process. There is no additional random noise (except the negligible quantization error due to digitization) and imperfections in the digital reconstruction stage. Therefore, digital reconstruction from optical in-line holograms, as given in previous sections, is a superior technique compared to the optical reconstruction.

The following pictures demonstrate the difference.

Figure 28. An optical reconstruction.

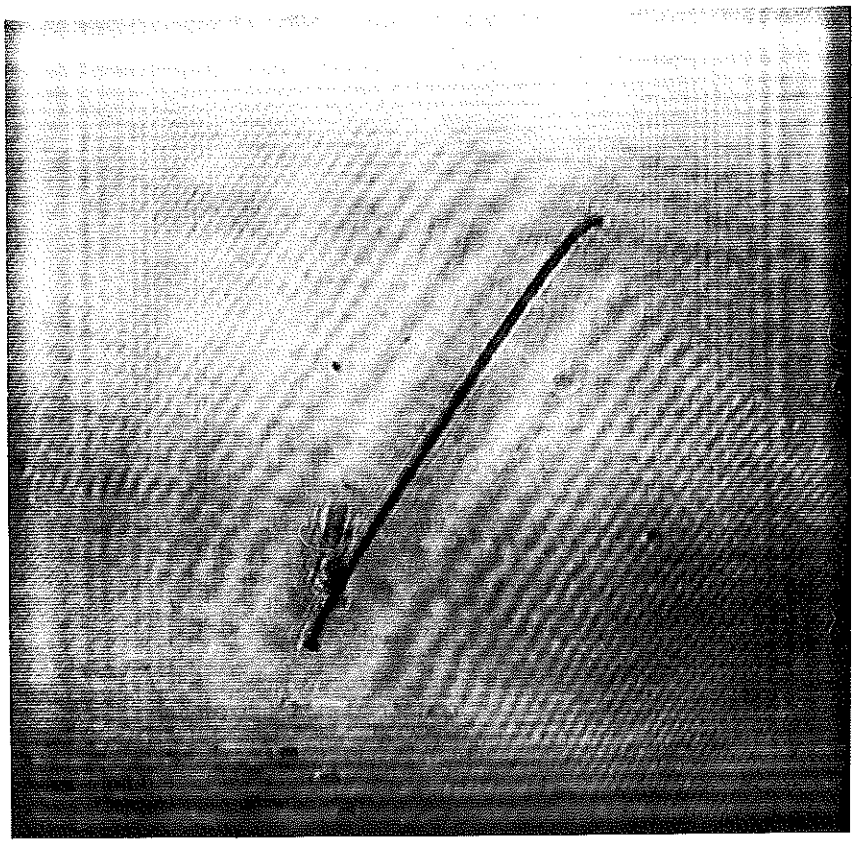

Figure 29. Digital reconstruction (Type I), corresponding to the optical reconstruction of Fig.28. $\alpha = 0.970$.

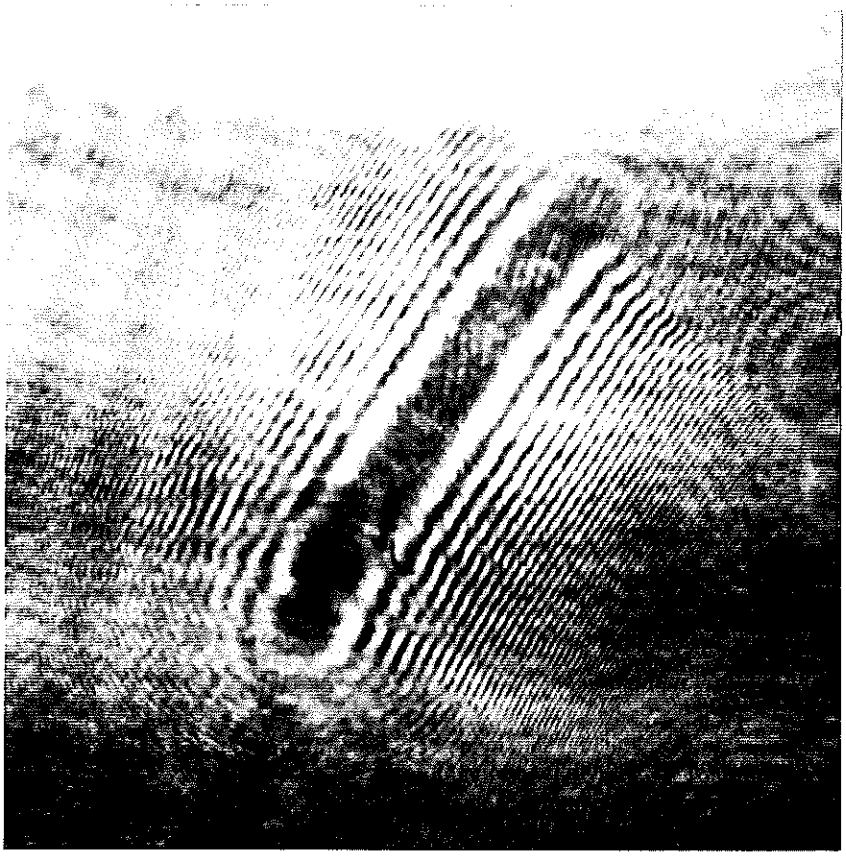

Figure 30. The digitized hologram portion from which the reconstruction of Fig.29 is obtained.

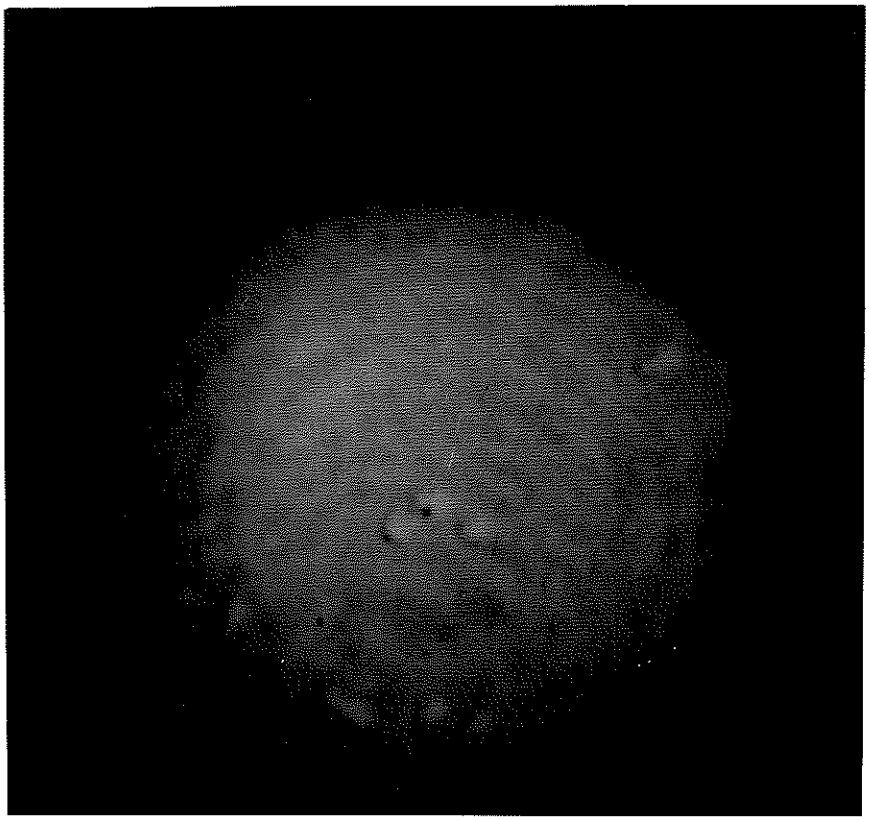

Figure 31. Another optical reconstruction.

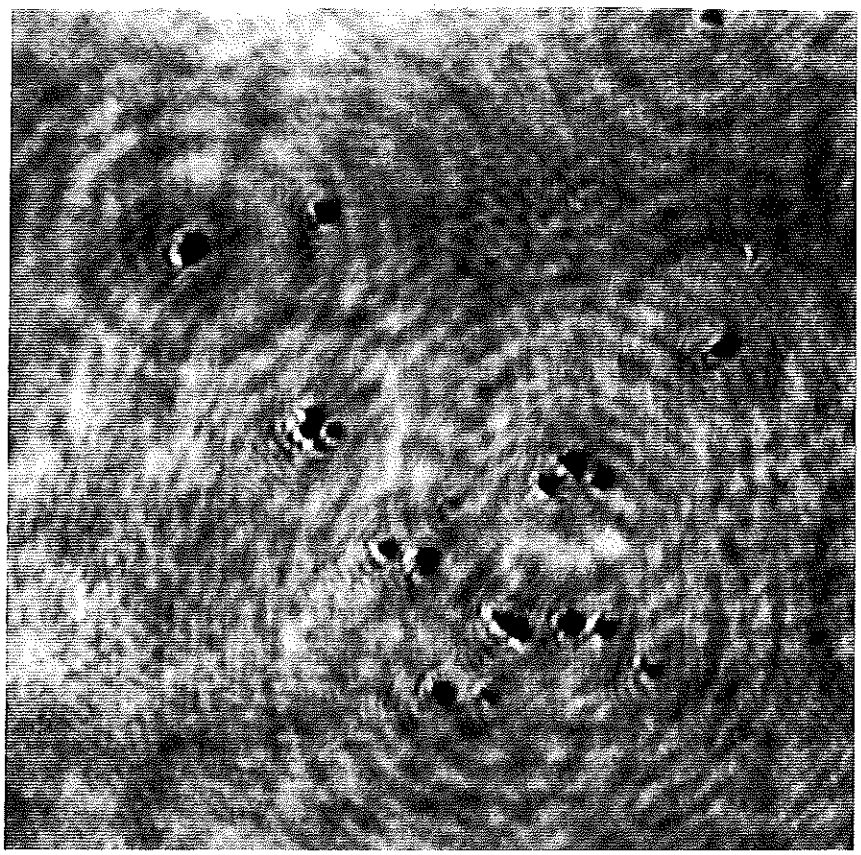

Figure 32. Digital reconstruction (Type I), corresponding to the optical reconstruction of Fig.31. $\alpha = 0.760$.

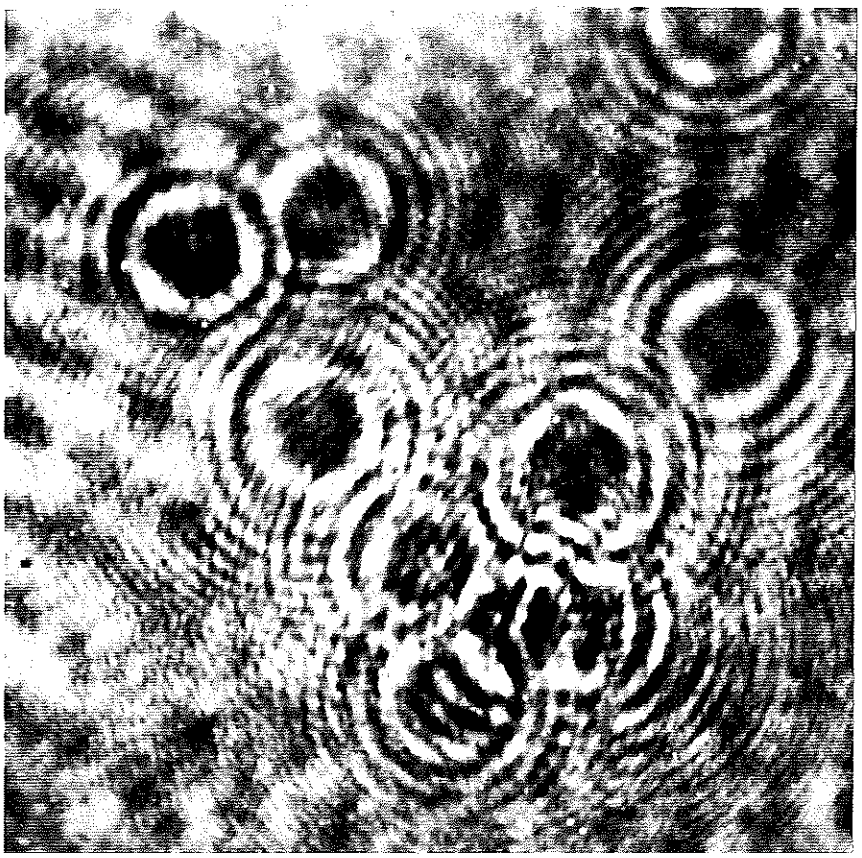

Figure 33. The digitized hologram portion from which the reconstruction of Fig.32 is obtained.

2.5. Multiexposure Holography Simulations

Multiexposure holograms are made by recording superpositions of many holograms. Thus, a multiexposure hologram $I(x,y)$ is given by,

$$I(x,y) = \frac{1}{K} \sum_{k=1}^{K} I_{z_k}(x,y) \ . \tag{2.64}$$

Since each individual hologram is given by (non-linear terms are assumed negligible, see eq.(2.7)),

$$I_{z_k} = 1 - a_k^*(x,y) ** h_{z_k}^*(x,y) - a_k(x,y) ** h_{z_k}(x,y) \ , \tag{2.65}$$

the multiexposure hologram becomes,

$$I(x,y) = 1 - \frac{1}{K} \sum_{k=1}^{K} \left[a_k^*(x,y) ** h_{z_k}^*(x,y) + a_k(x,y) ** h_{z_k}(x,y) \right] . \tag{2.66}$$

Reconstructions from this hologram are performed by reilluminating it with the same coherent plane wave, and imaging at a distance corresponding to one of the exposures, for instance z_j. In this case the reconstruction of $a_j(x,y)$ is superposed onto its twin-image, as discused in section 2. However, many additional terms are also produced in the reconstruction due to the other components of the multiexposure hologram. These are the so called "out of focus" reconstructions of object distributions located at planes other than z_j. Analytically,

$$\varphi_{z_j}(x,y) = 1 + I(x,y) ** h_{z_j}(x,y) ,$$

$$= 2 - \frac{1}{K} a_j^*(x,y) - \frac{1}{K} a_j(x,y) ** h_{2z_j}(x,y) - \tag{2.67}$$

$$\frac{1}{K} \sum_{\substack{k=1 \\ k \neq j}}^{K} \left[a_k^*(x,y) ** h_{z_k}^*(x,y) ** h_{z_j}(x,y) + a_k(x,y) ** h_{z_k}(x,y) ** h_{z_j}(x,y) \right] .$$

Using the properties,

$$h_{z_k}^*(x,y) ** h_{z_j}(x,y) = h_{z_j - z_k}(x,y) , \tag{2.68.a}$$

and,

$$h_{z_k}(x,y) ** h_{z_j}(x,y) = h_{z_j + z_k}(x,y) . \tag{2.68.b}$$

the reconstructed field, $\varphi_{z_j}(x,y)$, can be written as,

$$\varphi_{z_j}(x,y) = 2 - \frac{1}{K} a_j^*(x,y) - \frac{1}{K} a_j(x,y) ** h_{2z_j}(x,y) -$$

$$\frac{1}{K} \sum_{\substack{k=1 \\ k \neq j}}^{K} \left[a_k^*(x,y) ** h_{z_j - z_k}(x,y) + a_k(x,y) ** h_{z_j + z_k}(x,y) \right] . \tag{2.69}$$

From the formula above, it can be seen that the reconstruction has the desired object $a_j^*(x,y)$, and its twin-image. In addition to that, each single component of the

multiexposure hologram, other than $I_{z_j}(x,y)$, generates *two* additional terms which are themselves hologram fields: they correspond to hologram fields of $a_k(x,y)$ at distances $z_j - z_k$ and $z_j + z_k$, for each k. Among these hologram fields, the ones corresponding to small distances could be bothersome since they correspond to almost focused reconstructions.

2.5.1. Simulation Results

Some simulations are done using the Type I simulator of section 2.3.2. Fig.34 shows a simulated double exposure hologram of synthesized objects. One of the hologram components has the normalized hologram coefficient $\alpha = 1.1$, and the other one has $\alpha = 1.2$. (See section 2.3.2 for definition of α.) They are superposed using the image processor. Two reconstructions are obtained from the same hologram: one for $\alpha = 1.1$, and the other for $\alpha = 1.2$. The two reconstructions are shown in Figs.35 and 36. The four terms can be easily seen from each reconstructions. Two of them correspond to the focused object and its twin-image, whereas the other two are the holograms of the other object, at distances as formulated above.

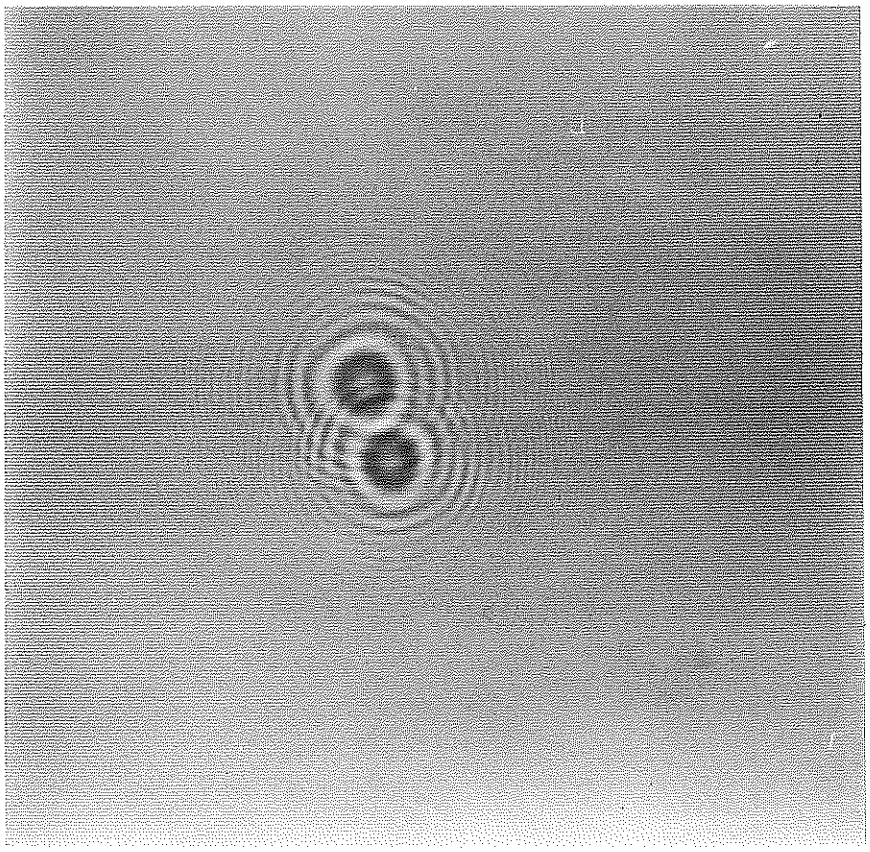

Figure 34. A simulated double exposure hologram.

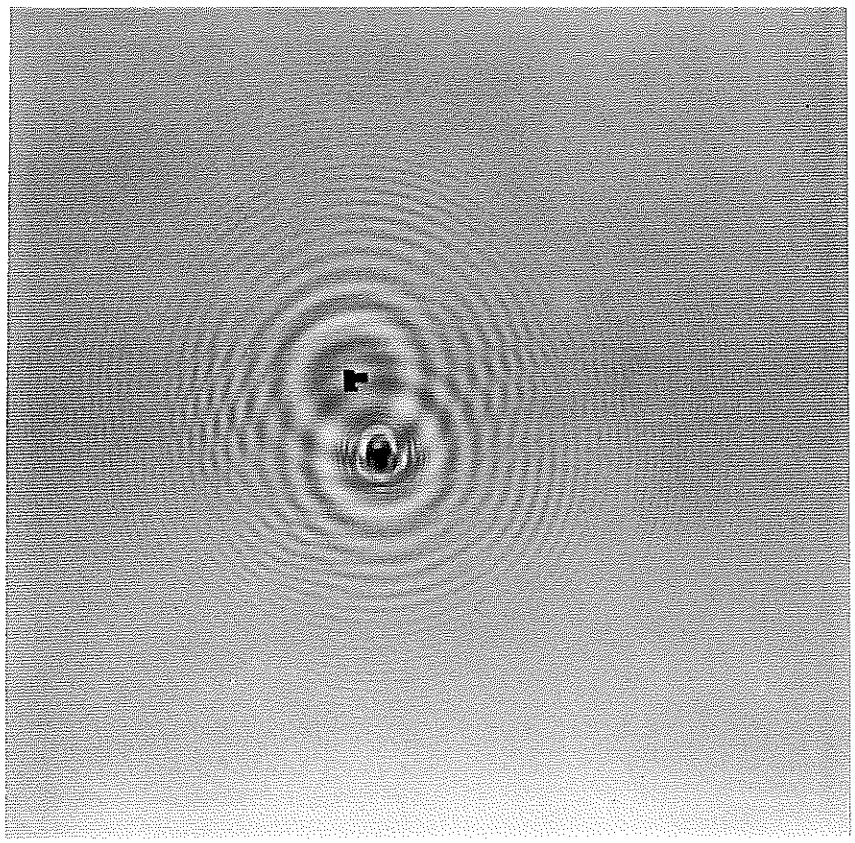

Figure 35. Reconstruction from the double exposure hologram of Fig.34. $\alpha = 1.1$.

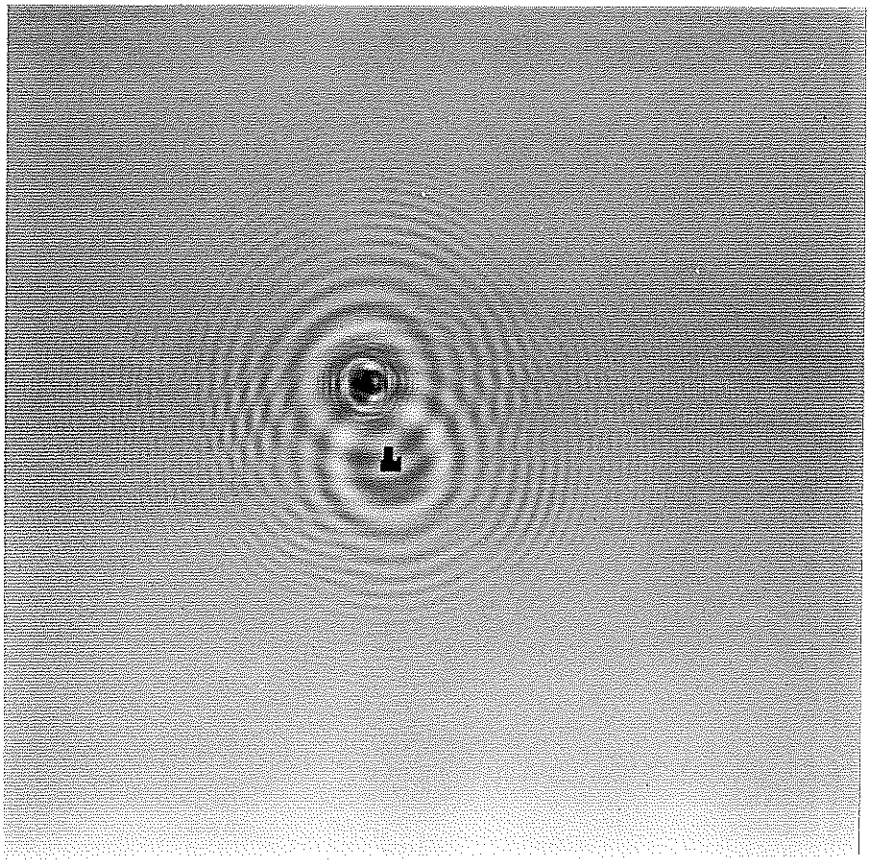

Figure 36. Reconstruction from the double exposure hologram of Fig.34. $\alpha = 1.2$.